Master's thesis
Particle Physics and Cosmology

Phenomenology and numerical analysis of the complex singlet extension of the Standard Model

Alex Stendahl

May 28, 2020

Supervisor(s): Prof. O.Lebedev

Censor(s): Prof. O.Lebedev
Dr. Mondal

UNIVERSITY OF HELSINKI
Particle Physics and Astrophysical Sciences

P.O. Box 4 (Yliopistonkatu 3)
FI-00014 University of Helsinki

It is often stated that of all the theories proposed in this century, the silliest is quantum theory. In fact, some say that the only thing that quantum theory has going for it is that it is unquestionably correct. -Professor M. Kaku

HELSINGIN YLIOPISTO — HELSINGFORS UNIVERSITET — UNIVERSITY OF HELSINKI

Tiedekunta — Fakultet — Faculty
Faculty of Science

Koulutusohjelma — Utbildningsprogram — Education programme
Particle Physics and Astrophysical Sciences

Tekijä — Författare — Author
Alex Stendahl

Työn nimi — Arbetets titel — Title

Phenomenology and numerical analysis of the complex singlet extension of the Standard Model

Opintosuunta — Studieinriktning — Study track
Particle Physics and Cosmology

Työn laji — Arbetets art — Level	Aika — Datum — Month and year	Sivumäärä — Sidoantal — Number of pages
Master's thesis	May 28, 2020	50 pages

Tiivistelmä — Referat — Abstract

The Standard model of particle physics has been very successful in describing particles and their interactions. In 2012 the last missing piece, the Higgs boson, was discovered at the Large Hadron Collider. However even for all its success the Standard model fails to explain some phenomena of nature. Two of these unexplained phenomena are dark matter and the metastability of the electroweak vacuum.

In this thesis we study one of the simplest extensions of the Standard model; the complex singlet scalar extension. In this framework the CP-even component of the singlet mixes with the Standard model like Higgs boson through the portal operator to form new mass eigenstates. The CP-odd component is a pseudo-Goldstone boson which could be a viable dark matter candidate. We analyse parameter space of the model with respect to constraints from particle physics experiments and cosmological observations.

The time evolution of dark matter number density is derived to study the process of dark matter freeze-out. The relic density of the Dark Matter candidate is then calculated with the `micrOmegas` tool. These calculations are then compared to the measured values of dark matter relic density.

Moreover, the electroweak vacuum can be stabilised due the contribution of the singlet scalar to the Standard Model Higgs potential. We derive the β-functions of the couplings in order to study the renormalisation group evolution of the parameters of the model. With the contribution of the portal coupling to the β-function of the Higgs coupling we are able to stabilise the electroweak vacuum up to the Planck scale. The two-loop β-functions are calculated using the SARAH tool.

Avainsanat — Nyckelord — Keywords
Standard model, Singlet extension, dark matter, electroweak vacuum

Säilytyspaikka — Förvaringsställe — Where deposited

Muita tietoja — övriga uppgifter — Additional information

Contents

Acknowledgements

I want to thank Professor O. Lebedev for his guidance, corrections and patience. I also want to thank Dr. S. Mondal for his invaluable help with the computer packages and the dark matter scans. I am also grateful to Dr. Venus Keus, Dr. Kimmo Tuominen and Dr. Matti Heikinheimo for the help they provided.

1. Introduction

Since the discovery of the Higgs boson [1] the particle physics Standard Model is complete in its particle content. The Standard model is a very successful theory [2] that describes the elementary particles and their interactions. For the reader's convenience, we briefly review the SM, and motivate theories beyond the SM, namely the complex singlet scalar extension.

The Standard Model has two types of particles, fermions and bosons. The bosons have integer spin and the fermions half integer spin. The fermions are commonly divided into two subgroups, leptons and quarks. The leptons, in a doublet representation, are written as

$$\begin{pmatrix} e \\ \nu_e \end{pmatrix}, \begin{pmatrix} \mu \\ \nu_\mu \end{pmatrix}, \begin{pmatrix} \tau \\ \nu_\tau \end{pmatrix} \tag{1.1}$$

where, e and ν_e are the electron and the electron neutrino, μ and ν_μ are the muon and muon neutrino, and τ and ν_τ are the tau and tau neutrino, respectively. Similarly we can write the quarks in the doublet representation as

$$\begin{pmatrix} u \\ d \end{pmatrix}, \begin{pmatrix} c \\ s \end{pmatrix}, \begin{pmatrix} t \\ b \end{pmatrix} \tag{1.2}$$

where u, d, c, s, t and b are the up, down, charm, strange, top and bottom quarks, respectively. The three lepton and quark doublets could also be referred to as three generations of leptons/quarks and have increasing mass compared to the same type of particle in the previous generation. As an example the top quark (3rd generation) is far heavier than the charm quark (2nd generation). The neutrino masses are still undetermined [3] but it has been shown that they have mass.

The Standard model is defined by an action. This action is a d-dimensional spacetime integral over the Lagrangian. We only consider four dimensional theories in this thesis. For a simple example we consider the free complex massive scalar field

$$\mathcal{S}_{scalar} = \int d^4x \mathcal{L}_{scalar} = \int d^4x \left[\partial_\mu \phi^* \partial^\mu \phi - m^2 \phi^* \phi\right]. \tag{1.3}$$

Free in this context means no interactions are present. The Lagrangian in eq.1.3 describes a spin 0 particle. The Lagrangian describing higher integer spin particles is a bit more complicated. The free fermions are described by the Dirac equation

$$\mathcal{L}_{fermions} = i\bar{\psi}\gamma^\mu \partial_\mu \psi - m\bar{\psi}\psi \tag{1.4}$$

where γ_μ are the gamma matrices. However an explicit mass term as in 1.4 is not allowed in the Standard Model due to the Standard model gauge invariance, but we will return to the fermion mass terms later.

Physical theories are usually invariant under certain transformations. For example the scalar field Lagrangian in eq.1.3, describing relativistic particles, is Lorentz invariant. It is also invariant under global phase transformation

$$\phi \to \phi' = e^{i\alpha}\phi. \tag{1.5}$$

We therefore impose symmetries on our theory and demand the action remain invariant under these transforms. The Lagrangian in eq.1.3 is not invariant under the transformation in eq.1.5 when the parameter α is position dependant, $\alpha(x)$, since the derivative term in eq.1.3 leaves behind a contribution proportional to $\propto \partial_\mu \alpha(x)$. To remain locally phase invariant we need to introduce the covariant derivative D_μ as

$$D_\mu = \partial_\mu + iqA_\mu \tag{1.6}$$

where the newly introduced gaugefield A_μ transforms as

$$A_\mu \to A'_\mu = A_\mu - \partial_\mu \alpha(x) \tag{1.7}$$

to cancel the extra term produced by the derivative of the transformation parameter. The locally phase invariant scalar field action is then

$$\mathcal{S}_{scalar} = \int d^4x \left[D^*_\mu \phi^* D^\mu \phi - m^2 \phi^* \phi \right] \tag{1.8}$$

with new interactions $\propto \phi^* \phi A_\mu A^\mu$. The same line of reasoning can be used when constructing the Standard Model Lagrangian which is symmetric under the gauge group

$$SU(3)_c \times SU(2)_L \times U(1)_Y \tag{1.9}$$

where $SU(3)_c$ is the symmetry group of strong interactions and $SU(2)_L \times U(1)_Y$ is the symmetry group of electroweak interactions.

These gauge groups have an associated representation for the particles, for example the $SU(2)_L$ gauge group is a 2×2 complex unitary group whose generators are 2×2 complex matrices obeying Lie algebra. Therefore particles that are $SU(2)_L$ symmetric have a fundamental representation as a doublet, like the ones displayed in 1.1. A singlet scalar is then a field that transforms trivially under the gauge group of the Standard Model. The model we introduce in the next chapter is a singlet under all Standard model gauge groups.

All these gauge groups have mediator particles that convey the interaction between particles. For QCD this particle is a gluon, for electroweak theory we have the spin-1 massive $W^\pm$ and Z-bosons and the massless photon, denoted by γ.

Unlike gauge bosons, for the Higgs we also have a $SU(2)_L \times U(1)_Y$ invariant potential. This potential is in the Standard model of the form

$$V_{Higgs} = -\frac{1}{2}\mu^2 H^\dagger H + \frac{1}{4}\lambda (H^\dagger H)^2 \tag{1.10}$$

that has a minimum when

$$\langle H^\dagger H \rangle = \frac{\mu^2}{\lambda} \equiv v^2 \tag{1.11}$$

and is defined as the Vacuum expectation value (VEV) of the Higgs field. This VEV spontaneously breaks the $SU(2)_L \times U(1)_Y$ symmetry to the $U(1)_{EM}$, so at this minimum the theory is no longer $SU(2)_L$ invariant. It is through this spontaneous symmetry breaking and the Yukawa interaction

$$\mathcal{L}_{Yukawa} = Y_f \bar{\psi} H \psi + h.c. \,, \tag{1.12}$$

where $h.c.$ denotes hermitian conjugate, that the fermions acquire mass in the Standard model. This can be understood if we expand the Higgs field in its real degrees of freedom in unitary gauge

$$\frac{1}{\sqrt{2}} \begin{pmatrix} 0 \\ h + v \end{pmatrix}. \tag{1.13}$$

We then get a term $\propto Y_f v \bar{\psi} \psi$ that is a fermion mass term similar to the one in 1.4

However even for the success of the Standard model there are still phenomena that it fails to explain. One of these is the existence of dark matter. This matter has only been observed through indirect means like gravitational lensing and the rotation curves of galaxies. Another question is if the potential 1.10 is stable or does it develop additional lower energy minima at some high energy. These are all questions the complex singlet extension will attempt to answer and complement the Standard model without needing exotic theories like Supersymmetry or String theory.

2. The model

The complex singlet extension of the Higgs is one of the simplest extensions of the Higgs sector. The extended sector consists of the Standard Model like Higgs and a additional complex singlet with two real degrees of freedom. Therefore the Lagrangian for the scalar sector is

$$\mathcal{L} = (D_\mu H)^\dagger (D^\mu H) + (\partial_\mu S)(\partial^\mu S^*) - V(H, S), \tag{2.1}$$

with H the Higgs doublet and S the Singlet. The D_μ is the covariant derivative. The general renormalizable global $U(1)$ symmetric potential $V(H, S)$ is

$$\begin{aligned} V(H,S) = &-\frac{1}{2}\mu^2 H^\dagger H + \frac{1}{2}\lambda_1 (H^\dagger H)(H^\dagger H) - \frac{1}{2}M_S^2 |S|^2 + \lambda_{SH}|S|^2 (H^\dagger H) \\ &+ \frac{1}{2}\lambda_S |S|^4. \end{aligned} \tag{2.2}$$

If the singlet acquires a VEV the $U(1)$-symmetry is spontaneously broken. This results in a massless Goldstone boson[4] being present in the particle spectrum. Since this is a phenomenologically disfavored situation we introduce an explicit soft $U(1)$-breaking term to the potential

$$V_{soft} = -\frac{\mu'^2}{4} S^2 + h.c. \tag{2.3}$$

in order to have a massive pseudo-Goldstone boson. Through a phase redefinition of the singlet soft mass term one can always have a real mass parameter. Therefore the potential we shall consider is henceforth

$$V_s = V(H, S) + V_{soft}. \tag{2.4}$$

In this potential the $U(1)$-symmetry is broken to $\mathbb{Z}_2$ by the VEVs we introduce later. The CP-odd component of the complex singlet is only ever pair produced so no decay channels exist. Later we shall put additional constraints on the theory.

For the model to correspond to measurements of the $W^\pm$ and Z-boson masses we require the H-field VEV to be nonzero. Furthermore we also consider the case when the additional scalar VEV is nonzero. We calculate the stationary points for the potential by treating $H^\dagger H$ and $S^* S$ as separate variables. Taking the derivative

and solving for both $H^\dagger H$ and $S^* S$ gives

$$\langle H^\dagger H \rangle = \frac{\lambda_S \mu^2 - \lambda_{SH}(M_S^2 + \mu'^2)}{2\lambda_1 \lambda_S - 2\lambda_{SH}^2} \equiv v^2, \tag{2.5}$$

$$\langle S^* S \rangle = \frac{\lambda_1 (M_S^2 + \mu'^2) - \lambda_{SH} \mu^2}{2\lambda_1 \lambda_S - 2\lambda_{SH}^2} \equiv v_s^2, \tag{2.6}$$

which we define as the VEVs for the respective fields.

Using the definition in 2.6 we expand the singlet around the VEV

$$S \to S = \frac{1}{\sqrt{2}}(\phi + i S_{DM} + v_s), \tag{2.7}$$

to obtain the CP-even term ϕ and the CP-odd term S_{DM} which will become our dark matter candidate. The particle S_{DM} is the pseudo-Goldstone boson. We also need to expand the gauge eigenstate H in terms of its VEV v. We rotate the H to the unitary gauge and expanding the H in terms of the field h and the VEV, since we have rotated away the three additional degrees of freedom in the doublet H. The additional degrees of freedom are in the $W^\pm$ and Z-bosons as longitudinal polarizations. The H field is then written as

$$H = \frac{1}{\sqrt{2}} \begin{pmatrix} 0 \\ h + v \end{pmatrix}. \tag{2.8}$$

The scalar potential is now in the gauge eigenstate basis (h, ϕ), but these are not the physical states, therefore we now consider the mixing of the two scalars. The two scalars mix in terms of gauge eigenstates to form mass eigenstates. The mixing can be inferred from the scalar potential and the masses written in matrix form. The M_h^2-matrix must therefore be diagonalized to get the physical (mass-) eigenstates for the model.

The mass matrix can be obtained by expanding the potential 2.4 in terms of the fields and the VEVs. The terms proportional to $1/2h^2$, $1/2\phi^2$ and $h\phi$ are then elements of the mass matrix for the CP-even fields.

The mass matrix in the gauge eigenstate basis is

$$M_h^2 = \begin{pmatrix} \lambda_1 v^2 & \lambda_{SH} v v_s \\ \lambda_{SH} v v_s & \lambda_S v_s^2 \end{pmatrix}, \tag{2.9}$$

which has the off diagonal terms $\lambda_{SH} v v_s$. This can then be diagonalized by the orthogonal transformation

$$M_{diag}^2 = (Z^H)^T M_h^2 Z^H, \tag{2.10}$$

to obtain the mass eigenstates. The orthogonal transformation matrix Z^H has the form

$$Z^H = \begin{pmatrix} \cos\theta & \sin\theta \\ -\sin\theta & \cos\theta \end{pmatrix}, \tag{2.11}$$

and the mixing angle θ satisfies

$$\tan 2\theta = \frac{2\lambda_{HS} v v_s}{\lambda_s v_s^2 - \lambda_1 v^2}. \tag{2.12}$$

The eigenvalues of the mass matrix are

$$m_{h_1}^2 = \frac{1}{2}\left(\lambda_1 v^2 + \lambda_S v_s^2 - \frac{\lambda_S v_s^2 - \lambda_1 v^2}{\cos 2\theta}\right), \tag{2.13}$$

$$m_{h_2}^2 = \frac{1}{2}\left(\lambda_1 v^2 + \lambda_S v_s^2 + \frac{\lambda_S v_s^2 - \lambda_1 v^2}{\cos 2\theta}\right), \tag{2.14}$$

corresponding to the two physical mass eigenstates h_1 and h_2. We also have a third mass eigenstate in the spectrum, the S_{DM}-state. The mass of this particle is $m_{S_{DM}}^2 = \mu^{'2}$ and it does not mix with the h_1 and h_2 states. We identify h_1 with the Standard model-like scalar with a mass $m_{h_1} = 125\text{GeV}$. The physical states are therefore mixed states of the gauge eigenstates. The mass eigenstates in terms of the gauge eigenstates are

$$h_1 = h\cos\theta - \phi\sin\theta \tag{2.15}$$

$$h_2 = \phi\cos\theta + h\sin\theta. \tag{2.16}$$

At the electroweak symmetry breaking scale we impose the constraint

$$\lambda_1\lambda_S - \lambda_{SH}^2 > 0 \tag{2.17}$$

$$\lambda_S,\ \lambda_1\ > 0 \tag{2.18}$$

since the mass matrix is a Hessian and we demand the determinant to be positive definite at electroweak scale. Imposing 2.17 and from 2.5 and 2.6 we obtain that the stationary points are local minima of the potential if

$$\lambda_S\mu^2 - \lambda_{SH}(M_S^2 + \mu^{'2}) > 0, \tag{2.19}$$

$$\lambda_1(M_S^2 + \mu^{'2}) - \lambda_{SH}\mu^2 > 0. \tag{2.20}$$

This local minimum exists even at loop level if radiative corrections are small.

After calculating the eigenvalues of the mass matrix we consider the free parameters of the model. In the Lagrangian we have

$$\mu^2,\ \mu^{'2},\ M_S^2,\ \lambda_1,\ \lambda_S,\ \lambda_{SH} \tag{2.21}$$

corresponding to the masses and the gauge eigenstate couplings. Further we impose the condition that $m_{h_1} = 125\text{GeV}$ to correspond to the 2012 scalar discovery [1]. Also we require $v = 246\text{GeV}$ to have correct gauge boson masses. These constraints leave only four free parameters, which we will choose to be

$$m_{h_2}^2,\ v_s,\ \theta,\ m_{S_{DM}}. \tag{2.22}$$

We will use these parameters when we calculate some processes in later chapters. However when we do computer analysis of the model to calculate relic density these parameters will not be used since the packages only use Lagrangian parameters.

3. Couplings and select processes

We shall now consider a few select processes in order to illustrate the deviation from the Standard Model. In general the phenomenology of the complex singlet extension resembles that of the Standard Model. We will consider the dark matter interactions with matter in order to show that it is naturally suppressed.

From the previous considerations it is first important to convert the Lagrangian parameters to the new parameters introduced in the model. This will however not work for `SARAH`[5] and `SPheno`[6] and by extension `micrOmegas`[7] since they work with Lagrangian parameters. After electroweak symmetry breaking the couplings can be expressed in terms of parameters related to the mass eigenstates instead of the gauge eigenstate parameters we begun with. The scalar potential after electroweak symmetry breaking in terms of mass eigenstates is too long to display here so only relevant terms are considered in this chapter.

The couplings λ_1, λ_S and λ_{SH} can be rewritten in terms of the chosen parameters: m_{h_2}, θ, $\mu^{'2}$, v_s. From the definition of the masses and using 2.12, the couplings can be written as

$$\lambda_1 = \frac{m_{h_1}^2}{v^2}\cos^2(\theta) + \frac{m_{h_2}^2}{v^2}\sin^2(\theta) \tag{3.1}$$

$$\lambda_S = \frac{m_{h_2}^2}{v_s^2}\cos^2(\theta) + \frac{m_{h_1}^2}{v_s^2}\sin^2(\theta) \tag{3.2}$$

$$\lambda_{SH} = \frac{m_{h_2}^2 - m_{h_1}^2}{2vv_s}\sin(2\theta). \tag{3.3}$$

with the detailed derivation in A.2.

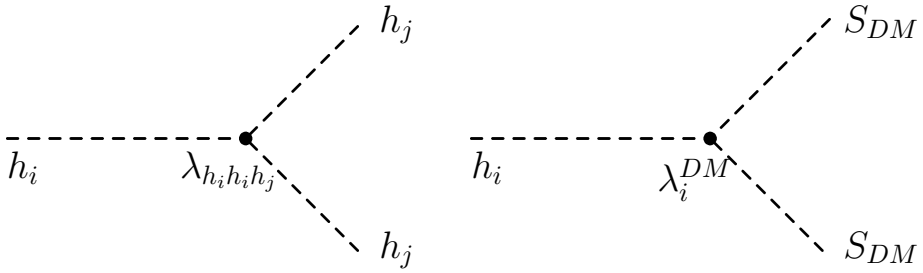

Figure 3.1: The trilinear scalar interaction (left). The dark matter - scalar interaction (right). All Feynman diagrams are drawn with `FeynMF`[8].

Four important vertices are the trilinear scalar interaction, scalar dark matter, the scalar-fermion and the scalar-gauge boson interactions. First the trilinear scalar

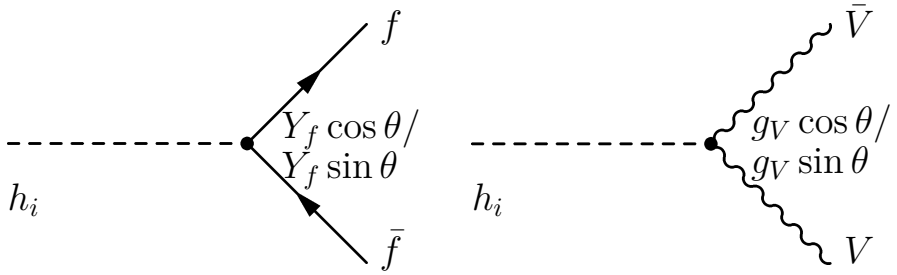

Figure 3.2: The scalar interaction with fermions (left). The scalar gauge boson interaction (right).

interaction has three contributions, the quartic singlet operator, the Higgs quartic operator and the portal. The coupling of the scalars can be obtained by taking the Lagrangian 2.3 and writing it in terms of mass eigenstates after spontaneous symmetry breaking. After the Lagrangian is expanded in terms of mass eigenstate we find terms proportional to $h_1 h_1 h_2$ and $h_1 h_2 h_2$. The obtained couplings can be simplified using 2.12 and the masses. We parametrize the interactions as

$$\mathcal{L}_{trilinear} = -\frac{v}{2}\sin\theta\lambda_{h_2h_1h_1}h_1^2h_2 - \frac{v_s}{2}\cos\theta\lambda_{h_2h_2h_1}h_2^2h_1, \tag{3.4}$$

then coupling for $h_2 h_1 h_1$ is found to be given by the expressions

$$\begin{aligned}\lambda_{h_2h_1h_1} =& \frac{1}{v^2 v_s}\Big(2m_{h_1}^2 v_s\cos^2\theta + m_{h_2}^2 v_s\cos^2\theta \\ &+2m_{h_1}^2 v\cos\theta\sin\theta + m_{h_2}^2 v\cos\theta\sin\theta\Big)\end{aligned} \tag{3.5}$$

and for $h_1 h_2^2$ it is

$$\begin{aligned}\lambda_{h_2h_2h_1} =& \frac{1}{v v_s^2}\left(2m_{h_2}^2 v_s\sin^2\theta + m_{h_1}^2 v_s\sin^2\theta\right. \\ &\left.-2m_{h_2}^2 v\cos\theta\sin\theta - m_{h_1}^2 v\cos\theta\sin\theta\right).\end{aligned} \tag{3.6}$$

If we let the heavier scalar eigenstate to have a mass greater than two of the lighter scalars then a new decay channel for the heavier mass eigenstate is introduced since it is kinematically allowed. This is gives a unique signal that could be verified experimentally in the form of four b-jet events or $h_2 \to (h_1^* h_1^*) \to \bar{b}b\tau^+\tau^-$-decays. Examples of these processes are displayed in figure 3.3.

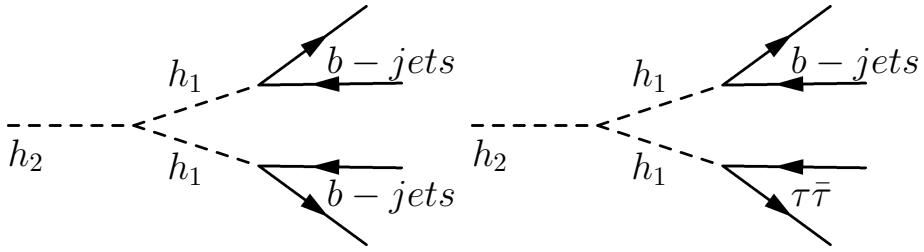

Figure 3.3: The heavier scalar decay to four b-jets (left), $\bar{b}b$ and $\tau\bar{\tau}$ (right)

The heavy scalar to Standard model-like Higgs decay width can be calculated from the trilinear couplings and is given by

$$\Gamma(h_2 \to h_1 h_1) = \frac{v^2 \sin^2\theta \lambda^2_{h_2 h_1 h_1} \sqrt{m^2_{h_2} - 4m^2_{h_1}}}{32\pi m^2_{h_2}} \tag{3.7}$$

where the coupling $\lambda_{h_2 h_1 h_1}$ is given by 3.5. The decay of the heavier scalar through the lighter mass eigenstate to fermions is naturally dependent on the scalar-fermion interaction. Since in this scalar extension the additional scalar gauge eigenstate does not couple to the fermionic sector directly due to gauge invariance, the Yukawa interaction is only rotated to the mass eigenstates by $H \to h_1 \cos\theta + h_2 \sin\theta$. The Yukawa interaction

$$\mathcal{L}_{Yukawa} = -Y_f \cos\theta f \bar{f} h_1 - Y_f f \bar{f} h_2 \sin\theta + h.c. \tag{3.8}$$

then has contributions from both mass eigenstates. The additional mass eigenstate coupling to fermions is suppressed by $\sin\theta$. The fermion masses are still at tree level $m_f = Y_f v$ but the Yukawa coupling measurements have a mixing angle dependence. The SM-like Higgs decay to fermions is then the same as in the SM

$$\Gamma = C \cos^2\theta \frac{g^2 m_f^2 m_{h_1}}{16\pi m_W^2} \left[1 - \frac{4m_f^2}{m_{h_1}^2}\right] \tag{3.9}$$

but with a small suppression of $\cos^2\theta$. The constant C is the color factor, $C = 1$ for leptons and $C = 3$ for quarks. We also have a identical process for the h_2 but suppressed by $\sin^2\theta$. While at tree level the fermion masses are unchanged at loop level the masses get corrections from both scalars [9], but this analysis is beyond the scope of this thesis.

The gauge boson couplings follow a similar pattern and the same reasoning as in the Yukawa couplings can be applied here. The $W^\pm$ couplings are

$$g_{W,h_1} = \frac{1}{2} g^2 v \cos\theta \tag{3.10}$$

$$g_{W,h_2} = \frac{1}{2} g^2 v \sin\theta \tag{3.11}$$

and the Z-boson couplings are

$$g_{Z,h_1} = \frac{1}{2} v (\sqrt{\frac{5}{2}} g' \sin\theta_W + g \cos\theta_W)^2 \cos\theta \tag{3.12}$$

$$g_{Z,h_2} = \frac{1}{2} v (\sqrt{\frac{5}{2}} g' \sin\theta_W + g \cos\theta_W)^2 \sin\theta. \tag{3.13}$$

We will calculate loop corrections from h_2 to the gauge boson masses later in this thesis.

Having introduced the coupling of the scalars to the matter sector attention can now be given to the dark matter candidate S_{DM} and its detectability. Since the

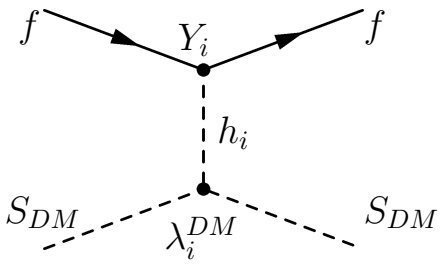

Figure 3.4: The direct detection Feynman diagram. At tree level it is a t-channel process mediated by one of the two scalars. The Yukawa coupling and the DM coupling indices relate to the mediated scalar.

dark matter candidate S_{DM} does not couple directly to the visible sector but only through the scalars $h_{1/2}$ the lowest order diagram corresponding to direct detection is the t-channel diagram3.4.

The coupling of S_{DM} to the scalars $h_{1/2}$ is obtained from the Lagrangian by writing the gauge eigenstates in terms of the mass eigenstates. The couplings can then be rewritten using expressions 3.1,3.2 and 3.3. We parametrize the scalar-dark matter couplings as

$$\mathcal{L}_{DM-scalar} = \frac{1}{2} v_s \lambda_1^{DM} S_{DM}^2 h_1 + \frac{1}{2} v_s \lambda_2^{DM} S_{DM}^2 h_2, \tag{3.14}$$

and the couplings are then given by

$$\lambda_1^{DM} = \frac{m_{h_1}^2}{v_s^2} \sin\theta \tag{3.15}$$

$$\lambda_2^{DM} = -\frac{m_{h_2}^2}{v_s^2} \cos\theta. \tag{3.16}$$

With these expressions the amplitude corresponding to 3.4 can be expressed by

$$|\mathcal{M}|^2 \propto \sin^2\theta \cos^2\theta \left(\frac{m_1^2}{t - m_1^2} - \frac{m_2^2}{t - m_2^2} \right)^2 \left(-\frac{1}{2} t + 2 m_f^2 \right) \tag{3.17}$$

which vanishes as $t \to 0$, giving a natural suppression of the direct detection rates for this model. It can therefore be concluded that the cross section of the dark matter candidate colliding with a nucleon is very small and therefore the direct detection rate is highly suppressed at small transferred momentum.

4. Experimental constraints

In this section we consider the consequences of the scalars mixing on the electroweak precision observables (EWPO) and the Higgs searches leading up to the discovery in 2012. The experiments provide constraints on the allowed parameters of the model. We will first consider corrections to the electroweak precision observables. These observables are measurements commonly used to constrain new models[10]. The EWPO were used even before the Higgs was discovered to constrain the allowed mass of the then undiscovered scalar.

We then consider constraints from the Higgs searches and the Higgs coupling measurements. Since the LHC had been searching for a scalar particle since its completion it is expected that some parameters are already ruled out by old experiments. We will see that at low mass ranges for the second scalar the Higgs searches and coupling measurements are the constraining factor. At high masses the EWPO provide the most stringent bounds.

4.1 EWPO

In the portal model corrections to electroweak theory enter at one loop level and come from modified couplings of the scalars to gauge bosons and different loop diagrams involving the two CP-even scalars. Some relevant loop diagrams are shown in fig.4.1. These new loops shift the couplings and gauge boson masses and we therefore need to compare the prediction of the complex singlet model to the accurately measured values of the electroweak theory in order to find the resulting bounds on the model parameters.

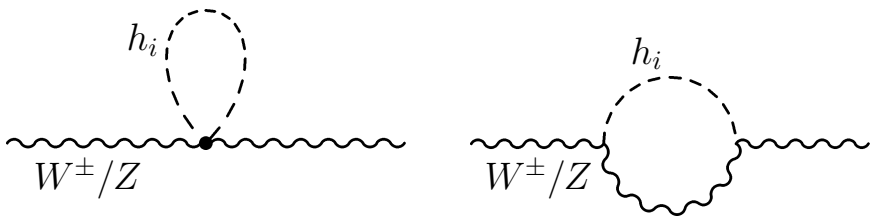

Figure 4.1: Examples of the gauge boson propagator loop corrections involving the scalar fields. Left: The quartic boson-scalar coupling loop. Right: The loop correction with trilinear couplings.

At one loop level, corrections involving the photon are zero. Calculating the

loop contributions to the gauge boson propagator gives

$$\delta\Pi_{VV}(p^2) = \frac{m_V^2 \sin^2\theta}{4\pi^2 v^2}\left(\frac{m_{h_2}^2 - m_{h_1}^2}{4}\left(\frac{1}{\epsilon}+1\right)\right. \tag{4.1}$$

$$\left. + \int_0^1 dx \left[m_V^2 - \frac{\Delta_2}{2}\right]\log\Delta_2 - \int_0^1 dx\left[m_V^2 - \frac{\Delta_1}{2}\right]\log\Delta_1\right), \tag{4.2}$$

Δ_i is defined by $\Delta_i = x m_{h_i}^2 + (1-x)m_V^2 - p^2 x(1-x)$ for the scalar h_i and the gauge boson V. In Δ_i the integration is done over the Feynman parameter x. The divergent part $1/\epsilon$ cancels in all physical observables and is not important for this study. This correction to the propagator modifies the masses of the gauge bosons but also the effective couplings of electroweak theory. The effective electroweak couplings can be expressed as [11], [12]:

$$g_{fZ}^{eff} = \frac{\sqrt{g_L^2 + g_Y^2}}{\sqrt{1 - \delta\Pi'_{WW}(m_W^2)}}\left(T_f^3 - Q_f s_{eff}^2\right), \tag{4.3}$$

$$s_{eff}^2 = \frac{g_Y^2}{g_L^2 + g_Y^2}\left(1 - \frac{g_L \delta\Pi_{\gamma Z}(m_Z^2)}{g_Y m_Z^2}\right), \tag{4.4}$$

$$g_W^{eff} = \frac{g_L}{\sqrt{1 - \delta\Pi'_{WW}(m_W^2)}} \tag{4.5}$$

g_L and g_Y being the $SU(2)_L$ and $U(1)$ gauge couplings respectively. The parameter s_{eff}^2 is defined from

$$\hat{A}_{LR} \equiv \frac{(\frac{1}{2} - s_{eff}^2)^2 - s_{eff}^4}{(\frac{1}{2} - s_{eff}^2)^2 + s_{eff}^4} \tag{4.6}$$

$\hat{A}_{LR}$ being the forward-backward asymmetry for a fermion. With the effective couplings some electroweak processes can be written in compact form. In this case the two interesting processes are the Z and W decay widths to fermions. With the effective couplings the decay widths are

$$\Gamma(Z \to \bar{f} f) = \frac{N_f m_Z}{24\pi}(g_{fZ}^{eff})^2 \tag{4.7}$$

$$\Gamma(W \to f' f) = \frac{N_f m_W}{48\pi}(g_W^{eff})^2. \tag{4.8}$$

Turning now to the coupling corrections, relying on [11] the corrections are calculated to be

$$\delta g_L = \frac{g_L}{g_L^2 - g_Y^2}\left(2\frac{\delta\Pi_{WW}(0)}{v^2} - 2\cos^2\theta_W \frac{\delta\Pi_{ZZ}(m_Z^2)}{v^2} + \frac{g_Y^2 \delta\Pi'_{\gamma\gamma}(0)}{2}\right), \tag{4.9}$$

$$\delta g_Y = \frac{g_Y}{g_L^2 - g_Y^2}\left(-\frac{2g_Y^2\delta\Pi_{WW}(0)}{g_L^2 v^2} + 2\sin\theta_W \frac{\delta\Pi_{ZZ}(m_Z^2)}{v^2} - \frac{g_L^2\delta\Pi'_{\gamma\gamma}(0)}{v^2} - \frac{g_L^2\delta\Pi'_{\gamma\gamma}(0)}{2}\right), \tag{4.10}$$

$$\delta v = \frac{-2v\Pi_{WW}(0)}{g_L^2 v^2}. \tag{4.11}$$

With these corrections the shifts in electroweak results can be calculated to see if experimental data agrees with the extension. To simplify the calculations only leading order terms in Π_{VV} are considered, also noteworthy is that in this model $\delta\Pi_{\gamma\gamma}$ are zero. The loop corrections are modified from the Standard model case, and it is therefore imperative to compare the predicted EWPO to the measured ones. If the additional contributions cause the predicted value to deviate from measured ones the model is discarded. This is done by comparing the predicted quantity to the measured one using a χ^2-distribution

$$\chi^2((m_{h_2}), \sin\theta_i) = \sum_i \frac{(O_i^{ex} - O_i^{th}((m_{h_2}), \sin\theta))^2}{(\sigma_i^{ex})^2} \tag{4.12}$$

where O_i^{ex} is the experimentally measured value, σ_i^{ex} its error and O_i^{th} the predicted value. By minimizing the χ^2 distribution we can exclude regions by satisfying

$$\chi^2((m_{h_2}), \sin\theta) - min\left[\chi^2((m_{h_2}), \sin\theta)\right] < 3.84 \tag{4.13}$$

giving a 95% confidence interval for the parameters. These constraints can then be plotted in a contour plot to show the excluded regions.

A simple method of estimating the excluded regions is by using Peskin-Takeuchi S, T and U parameters [13]. The relevant parameters are S and T, which are given in this model by

$$S = \frac{16\pi \cos^2\theta_W \Pi'_{ZZ}(0)}{g^2}, \tag{4.14}$$

$$T = \frac{4\pi}{e^2}\left(\frac{\delta\Pi_{WW}(0)}{m_W^2} - \frac{\delta\Pi'_{ZZ}(0)}{m_Z^2}\right). \tag{4.15}$$

If $m_{h_2} \gg m_{h_1}$ these simplify to

$$S \approx \frac{\sin^2\theta}{6\pi}\log\frac{m_{h_2}}{M_S} \qquad\qquad T \approx -\frac{3\sin^2\theta}{8\pi\cos^2\theta_W}\log\frac{m_{h_2}}{M_T} \tag{4.16}$$

for $M_T \approx 211$GeV and $M_S \approx 81$GeV. The limits from the oblique parameters can be calculated [14] using

$$(\chi^2_{STU})_i = x^T C^{-1} x,\ x^T = (S_i - \hat{S}, T_i - \hat{T}, U_i - \hat{U}). \tag{4.17}$$

Assuming $U = 0$ the covariance matrix C is

$$C = \begin{pmatrix} 8.1 & 5.733 \\ 5.733 & 4.9 \end{pmatrix} \times 10^{-3} \Rightarrow C^{-1} = \begin{pmatrix} 718.19 & -840.28 \\ -840.28 & 1187.2 \end{pmatrix} \tag{4.18}$$

and $\hat{S} = 0.06, \hat{T} = 0.10$ [15]. We then require $\chi^2_{ST} < 8.025$ to be within 2σ of the measured values. These parameters give a good indication for heavy scalars but the analysis contained within [11] is more comprehensive and is valid for all scalar mass ranges. However the S,T and U parameters are a quick way to probe large

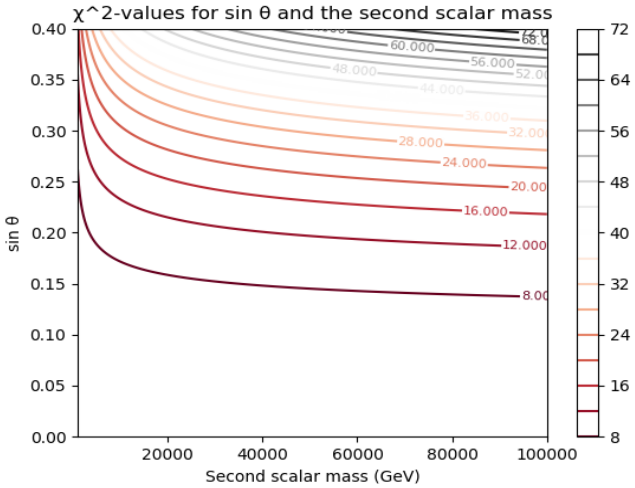

Figure 4.2: Peskin–Takeuchi parameter constraints for the mixing angle θ and the second scalar mass. We require $\chi^2 < 8.025$.

mass ranges, but should not be solely depended upon, especially in their simplified form. Using a simple Python script we can plot the constraints from the S and T parameters in a contour plot. In figure 4.2 the values of $\sin\theta \in [0, 0.4]$ and $m_{h_2} \in [1000\text{GeV},\ 100\text{TeV}]$ are plotted to constrain the $\sin\theta$ and second scalar mass ranges. However for the lower mass range the condition $m_{h_1} \ll m_{h_2}$ is suspect. Evidently for the high mass ranges the value of the mixing angle must be below $\sin\theta \leq 0.15$.

The work done in [11] shows that the limits from electroweak precision measurements are non trivial for scalar masses $m_{h_2} < 60\text{GeV}$ and $m_{h_2} > 170\text{GeV}$ and only increase as the scalar mass increases. This agrees well with the Peskin–Takeuchi parameters S and T scans since they correspond to loop corrections to electroweak processes.

4.2 Higgs coupling measurements

Since the scalars mix together as previously discussed the scalar sector is modified from the Standard model case. The mixing modifies the coupling of the Standard model-like Higgs to gauge bosons and fermions. The additional scalar therefore contaminates the Standard model like Higgs h_1 signal strengths. We only consider the channels $h_1 \to 4l$ and $h_1 \to \gamma\gamma$ since these processes have the best mass resolution. The expected signal strength of the extended model can be compared to the measured value. For the Standard Model the signal strength is defined to be $\mu = 1$. The measured values are displayed in table 4.2

Channel	μ (ATLAS)	μ (CMS)
$h_1 \to \gamma\gamma$	$1.17^{+0.27}_{-0.27}$	$1.12^{+0.24}_{-0.24}$ [16]
$h_1 \to ZZ^* \to 4l$	$1.44^{+0.40}_{-0.33}$	$1.00^{+0.29}_{-0.29}$ [16]

Using recent measurements and including a 15% theoretical prediction error, the limit

$$\mu > 0.81,\ 95\%\ CL \tag{4.19}$$

is obtained for the signal strength. The constraint on $\sin\theta$ when $m_{h_2} \geq \frac{1}{2}m_{h_1}$ is found to be [11]:

$$\sin\theta < 0.44,\ 95\%\ CL. \tag{4.20}$$

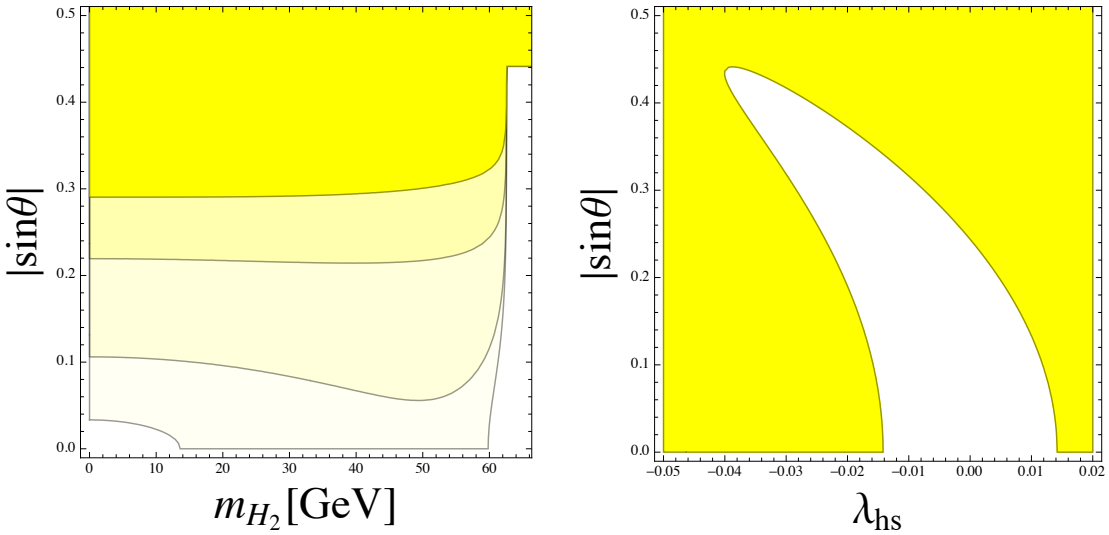

Figure 4.3: Exclusion regions for $m_{h_2} < 65$GeV from the Higgs coupling measurements (left). From lightest to darkest the portal coupling λ_{SH} is $-0.011, 0.0001, 0.011, 0.014$. The excluded region for $m_{h_2} = 20$GeV (right). The white area is where the $h_1h_2h_2$-coupling 3.5 is very small [11].

When the second scalar h_2 has a mass less than half of the SM-like Higgs a new decay channel for the SM-like Higgs is kinematically allowed. This puts stronger constraints on $\sin\theta$ than before since it modifies the Higgs decay branching ratios. These constraints are plotted in 4.3. Therefore at light h_2 the portal coupling λ_{SH} is effectively limited to values $|\lambda_{SH}| < 0.015$. However for negative λ_{SH} one can adjust the coupling so that the decay $h_1 \to h_2h_2$ vanishes.

4.3 Direct Higgs searches

Further constraints on the additional scalar can be obtained from Higgs-like searches at LEP and LHC. The following searches are taken into account[11]:

- $h_2 \to \gamma\gamma$ at ATLAS [17] and CMS [18]
- Limits from $h_2 \to ZZ$ and $h_2 \to WW$ searches in CMS for $m_{h_2} > 145\text{GeV}$ [19],
- Searches of $h_2 \to ZZ$ in $4l$-channel for $m_{h_2} < 145\text{GeV}$ in both CMS[20] and ATLAS [21],
- h_2 decays to $h_2 \to h_1 h_1$ with $\hat{b}b\gamma\gamma$ final states in CMS [22] and ATLAS [23],
- h_2 decays to $h_2 \to h_1 h_1$ with $\hat{b}b\hat{b}$ final states [24] in CMS,
- LEP searches for the Higgs (primarily $h_2 \to \hat{b}b$ decays)[25],
- DELPHI searches for a light Higgs by Z-decays[26],
- b-physics constraints on light Higgs [27] [28].

These experiments provide the most stringent constraints on the additional scalar mass and the mixing angle when $m_{h_2} < 450\text{GeV}$, except for a few isolated regions where the coupling measurements are more limiting. For extremely low masses $m_{h_2} < 5\text{GeV}$ the constraints from $B \to Kll$ are the dominating ones. In the mass range $5\text{GeV} < m_{h_2} < 12\text{GeV}$ the b-physics in [27] and light scalar searches in [26] provide the dominant contributions, limiting $\sin\theta < 0.5$. In the mass ranges above 12GeV up to 115GeV the Higgs searches in [25] are the relevant experiments limiting the angle to $\sin\theta \sim \mathcal{O}(10^{-1})$. When the mass of the additional scalar is $120\text{GeV} < m_{h_2} < 130\text{GeV}$ the constraints are loose due to the SM-like Higgs and their shared interaction types. Just above and below these masses the diphoton searches dominate [17][18]. Above 135GeV the electroweak decays $h_2 \to WW$ and $h_2 \to ZZ$ are the most relevant. Searches in [29],[19] and [20] provide the most stringent limits in this region, limiting $\sin\theta$ to $\sin\theta < 0.3 - 0.4$ depending on the mass of h_2. At mass ranges above 450GeV the oblique corrections become the constraining factor.

The limits discussed are modified depending on the value of the portal coupling λ_{SH}. Especially if the decay $h_1 \to h_2 h_2$ is kinematically allowed the Higgs signal strength would decrease in this model. If the second scalar can decay to two SM-like Higgs the dependence on λ_{SH} gives a suppression of the $h_2 \to WW$ and $h_2 \to ZZ$ decays with the $h_2 \to h_1 h_1$ decay becoming more prominent. These effects only become significant for $\lambda_{SH} > 1$, and in general the direct Higgs searches and coupling measurements provide more conservative limits on $m_{h_2}, \sin\theta$. When the Higgs decay to h_2 is kinematically allowed this decay would dilute the signal strength in 4.2. In the region $m_{h_2} > 2m_{h_1}$ the λ_{SH} dependence on the limits become relevant since the decay $h_2 \to ZZ/W^{\pm}W^{\mp}$ become less favorable than the decay $h_2 \to h_1 h_1$ as λ_{SH} increases. It is however only relevant when $\lambda_{SH} \gtrsim 1$ and only becomes the leading constraint when $\lambda_{SH} \gtrsim 2$.

4.4 Summary of the constraints

We conclude this chapter by summarizing the limits by experiments and theoretical predictions. When $m_{h_2} \sim \mathcal{O}(1)$GeV the Higgs coupling measurements limit the mixing angle to $\sin\theta < 0.45$ and the massless case is ruled out completely by Higgs direct searches. In the lower mass range 10GeV $\leq m_{h_2} \leq$ 90GeV the model is stringently constrained by the Higgs direct searches, limiting $\sin\theta$ to be below $\sin\theta \simeq 0.15$. Approaching the Standard Model like Higgs mass of 125GeV from the lower mass region the mixing angle is limited by Higgs coupling measurements to $\sin\theta \lesssim 0.45$. At the Standard Model like Higgs mass the constraints are loose allowing for a nearly degenerate second scalar.

At higher masses $m_{h_2} >$ 125GeV the Higgs direct searches variably rule out mixing angles in the range $\sin\theta \sim 0.2 - 0.4$ depending on the second scalar mass. Finally at masses above 450GeV the EWPO measurements and the S,T parameters constrain the model in a monotonically increasing way from $\sin\theta \sim 0.3$ down to $\sin\theta \leq 0.15$ as the second scalar mass increases. Since in a later chapter we will use this additional scalar and the scalar mixing to stabilize the electroweak vacuum the higher mass ranges are especially of interest. The summary of these results is plotted in fig 4.4.

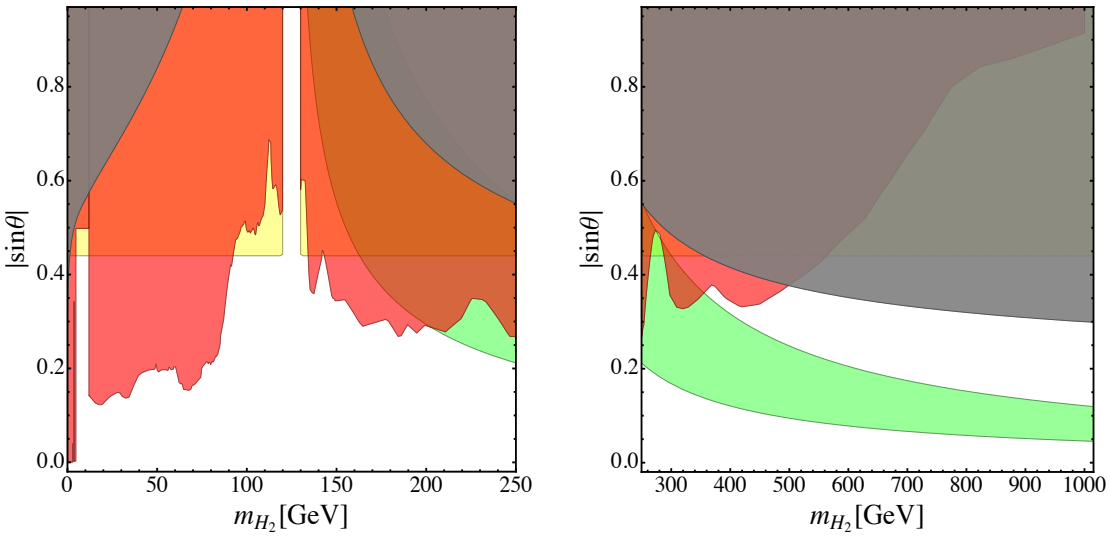

Figure 4.4: Left: Excluded parameter space in the range 0GeV $\leq m_{h_2} \leq$ 250GeV. The red area is direct searches exclusion, EWPO in gray and Higgs coupling measurements in yellow. The green region is favoured by electroweak vacuum stability when $\lambda_{SH} = 0.01$[11]. Right: The mass range 250GeV $\leq m_{h_2} \leq$ 1000GeV.

5. Dark Matter

The existence of dark matter is a well established fact in modern physics. Dark matter is used to explain some phenomena that the Standard model cannot account for. One of these phenomena is the discrepancy between classically predicted and measured values for galaxy rotation curves. As an example the rotation of the M33 galaxy[30] is too fast at the outer edges for classical models to account for. A common explanation for this phenomenon is the existence of additional matter that is as of today of unknown type. Dark matter interacts gravitationally and this interaction is one of the primary channels for observing matter through gravitational lensing. Gravitational lensing is the phenomenon where light from a distant source is bent due to a massive object in the vicinity of the lights path. The rest of dark matter interactions remain unknown.

Direct detection experiments work by measuring signals of particles colliding as we move through space and therefore through a dark matter "wind"[31]. When moving through this dark matter wind some dark matter particles would collide with nuclei leaving a signal in these types nuclei collision experiments. These kind of direct detection experiments usually operate in momentum exchange ranges of $\sqrt{t} \approx 20-200keV$[31]. In some models, as in the current model of pseudo-Goldstone dark matter, this direct detection amplitude is suppressed leading to no expected signals with current sensitivities.

The indirect detection experiments search for DM interactions resulting in visible SM final states [32]. This process is the annihilation of dark matter into Standard model final states. These kind of experiments need to distinguish between a potential dark matter candidate and astrophysical background. In the complex singlet extension, processes resulting in SM final states involve the CP-even scalars as mediators that then couple to the SM.

All these detection experiments put constraints on any DM candidate. In order to study the required phenomenology the most important quantity is relic density or relic abundance Ωh^2. By convention the parameter h is included. The parameter h is the rate of expansion of the universe in terms of $100km/s/Mpc$, i.e if $h = H_0$, then $h \approx 0.674$[33],[34]. The critical energy density ρ_{crit} is the required energy density of the universe to obtain a flat universe. It can be found from the first Friedman equation[35]

$$H^2 = \frac{8\pi G}{3} + \frac{\Lambda c^2}{3} - \frac{Kc^2}{a^2} \tag{5.1}$$

for $K = 0$. The critical density at present value[34] is

$$\rho_{critical} = 1.878 \times 10^{-29} h^2 \frac{g}{cm^3} \approx 8.531 \times 10^{-30} \frac{g}{cm^3} \tag{5.2}$$

This critical density is then related to the Ω parameter as

$$\Omega_i = \frac{\rho_i}{\rho_{critical}} = \frac{8\pi G}{3H^2}\rho_i = \frac{\rho_i}{1.878 \times 10^{-29} h^2} \tag{5.3}$$

making it obvious why the h^2 is included in literature when reporting relic densities. From surveys like the `PLANCK` mission the value for cold dark matter relic density has been measured and is presently [34]

$$\Omega h^2 = 0.120 \pm 0.001. \tag{5.4}$$

We can then calculate the energy density for dark matter by inverting the relation 5.3, resulting in a energy density of

$$\rho_c = (2.25 \pm 0.02) \times 10^{-30} \frac{g}{cm^3} \tag{5.5}$$

This energy density is the third and last requirement for our DM candidate, but we will refer to 5.4 since it is the format of [34].

5.1 Freeze-out

To be able to interpret the dark matter calculation results we first need to familiarize ourselves with the governing equations of dark matter evolution and the mechanisms therein. For weakly interacting massive particles (WIMPS) the mechanism is called freeze out or decoupling.

Take a particle that in the early universe was in thermal equilibrium, i.e the annihilation and production of the DM candidate is initially in equilibrium. The number density n of the DM candidate is therefore proportional to the temperature cubed, $n \propto T^3$. Approximating the particle soup as a weakly interacting gas the particle statistics are described by the distribution function

$$f(E, \mu, T) = \frac{1}{e^{\beta(E-\mu)} \pm 1} \tag{5.6}$$

with the chemical potential denoted by μ, the energy E and $+$ sign for fermions and $-$ sign for bosons. The number density in thermal equilibrium is

$$n_{eq} = \int \frac{d^3p}{(2\pi)^3} g f(E, \mu, T) \tag{5.7}$$

the distribution function having a implicit momentum dependence in E[1], g is the number of degrees of freedom of the particle (spin, polarization etc.), also called the

[1] $E = \sqrt{\hat{p}^2 + m^2}$

degeneracy of the energy level. In the high temperature limit $T \gg m$ for the particle mass m, the particle number density is proportional to the temperature cubed $\propto T^3$. When the the universe cools the number density gets suppressed by the Boltzmann factor. Neglecting the chemical potential the particle densities are proportional to

$$n_{eq} \propto T^3, \;\; T \gg m \tag{5.8}$$

$$n_{eq} \propto (mT)^{\frac{3}{2}} e^{-m\beta}, \beta = (k_B T)^{-1}, \;\; T \ll m \tag{5.9}$$

with the second term having the suppression of the Boltzmann factor. Because the cooling is accompanied by the expansion of the universe the statement of thermal equilibrium is more involved than in the classical sense of time independent state. However the expansion rate is usually slow compared to interaction rates and can be treated as an adiabatic process.

As the universe expands and cools the DM annihilation processes become increasingly rare. This process leads to freeze out, after which the dark matter falls out of thermodynamic equilibrium and total dark matter particle number is conserved. It is this process which is the most popular mechanism for explaining the observed relic abundance today [36].

5.2 Boltzmann equation

To understand dark matter production and relic density we need to look at the governing equation of freeze-out. Then by extension we gain some insight into what `micrOmegas` does. In general the dynamics of a system is described by the Boltzmann equation. It takes the form [37],

$$\mathbb{L} f(t, E) = \mathbb{C}(f(t, E)) \tag{5.10}$$

with the Liouville operator $\mathbb{L}$ and the collision term $\mathbb{C}$. The general form of $\mathbb{L}$ is

$$\mathbb{L} = \left(p^\nu \frac{\partial}{\partial x^\nu} - \Gamma^\mu_{\alpha\beta} p^\alpha p^\beta \frac{\partial}{\partial p^\mu} \right) \tag{5.11}$$

where the connection Γ is the Christoffel symbol. For non-relativistic cases the Liouville operator simplifies to a total derivative

$$\mathbb{L} = \frac{d}{dt} = \left(\frac{\partial}{\partial t} + \frac{dx_\mu}{dt} \frac{\partial}{\partial x_\mu} + \frac{dp_\nu}{dt} \frac{\partial}{\partial p_\nu} \right). \tag{5.12}$$

By integrating 5.10 over the three momentum an equation for the number density time evolution is obtained as[38]

$$\frac{dn}{dt} = \hat{\mathbb{C}}(f(t, E)) - 3Hn \tag{5.13}$$

for the Hubble parameter $H = \dot{a}(t)/a(t)$ that describes the expansion rate. The collision part $\hat{\mathbb{C}}(f(t, E))$ is now integrated, as denoted by the hat. If the collision operator is zero then the number density is $n(t) \propto a^{-3}$, which is expected. For a general collision process $a + b ... i \rightarrow \alpha + \beta ... \omega$ the relevant part of the collision operator is given by

$$\hat{\mathbb{C}}_i = -\int \frac{g_a d^3p_a}{(2\pi)^3 2E_a}\frac{g_b d^3p_b}{(2\pi)^3 2E_b}...\frac{g_\alpha d^3p_\alpha}{(2\pi)^3 2E_\alpha}\frac{g_\beta d^3p_\beta}{(2\pi)^3 2E_\beta}...(2\pi)^4\delta^4(p_a + p_b... - p_\alpha - p_\beta...) \tag{5.14}$$

$$S\left(|\mathbb{M}_{a+b...\to\alpha+\beta...}|^2 f_a f_b... f_i(1 \pm f_\alpha)(1 \pm f_\beta)...(1 \pm f_\omega)\right. \tag{5.15}$$

$$\left. -|\mathbb{M}_{\alpha+\beta...\to a+b...}|^2 f_\alpha f_\beta... f_\omega(1 \pm f_a)...(1 \pm f_i)\right). \tag{5.16}$$

for the internal degrees of freedom g, the symmetry factor S and the squared matrix element $|\mathbb{M}_{i+j...\to\delta+\Delta...}|^2$. In the equation above the plus(minus) sign corresponds to bosons(fermions). The symmetry factor takes into account exchanges of identical particles. Now assuming Charge conjugation - Parity (CP) is conserved we can simplify the two latter lines, eq.5.15 and 5.16. This leads to the two processes matrix elements are approximately equal, we can therefore denote both matrix elements as $|\mathbb{M}|^2$. We also assume that the particle density for the final states are low meaning $f(t, E) \ll 1$, simplifying $f(t, E) \pm 1 \approx \pm 1$. With these assumptions the collision term is shortened to

$$\hat{\mathbb{C}}_i = -\int \frac{g_a d^3p_a}{(2\pi)^3 2E_a}\frac{g_b d^3p_b}{(2\pi)^3 2E_b}...\frac{g_\alpha d^3p_\alpha}{(2\pi)^3 2E_\alpha}\frac{g_\beta d^3p_\beta}{(2\pi)^3 2E_\beta}... \tag{5.17}$$

$$(2\pi)^4\delta^4(p_a + p_b... - p_\alpha - p_\beta...)S|\mathbb{M}_{a+b..\to\alpha+\beta...}|^2\left(f_a f_b... f_i - f_\alpha f_\beta... f_\omega\right). \tag{5.18}$$

To obtain the final result for the number density time evolution in an expanding universe we look at a specific process, in this case the collision $S_{DM} + S_{DM} \to f + \hat{f}$. The symmetry factor is $S = 1$ since we lose two DM particles which is compensated by two identical particles in the initial state. The temperature range we are interested in is $T \gg m_f$ and $T \lesssim m_{DM}$. In this region the fermions and bosons distributions can be described by Boltzmann distribution factors $e^{-m/T}$ instead of their respective distribution functions $(e^{-m/T} \pm 1)^{-1}$.

We can describe the dark matter distribution function with Boltzmann factors, and we can also assume the fermions $f, \bar{f}$ are in thermodynamic equilibrium. This combined with the conservation of momentum gives

$$f_{1,eq} f_{2,eq} = e^{-(E_1+E_2)/T} = f_{\bar{f}} f_f = e^{-(E_{\bar{f}}+E_f)/T}, \tag{5.19}$$

where the distributions $f_{1,eq}$ and $f_{2,eq}$ are the dark matter distribution functions if they were in thermal equilibrium. Taking this result and accounting for the symmetry factor we write the collision operator as

$$\hat{\mathbb{C}}_i = -\int \frac{g_1 d^3p_1}{(2\pi)^3 2E_1}\frac{g_2 d^3p_2}{(2\pi)^3 2E_2}(f_{DM,1} f_{DM,2} - f_{1,eq} f_{2,eq}) \tag{5.20}$$

$$\left(\int \frac{g_a d^3p_a}{(2\pi)^3 2E_a}\frac{g_b d^3p_b}{(2\pi)^3 2E_b}(2\pi)\delta^4(\sum_i p_i)|\mathbb{M}_{1+2\to3+4}|^2\right). \tag{5.21}$$

The second part 5.21 is the expression for the cross section. Simplifying the collision term we get

$$\hat{\mathbb{C}}_i = -\int \frac{g_1 d^3p_1}{(2\pi)^3 2E_1}\frac{g_2 d^3p_2}{(2\pi)^3 2E_2}(f_{DM,1} f_{DM,2} - f_{1,eq} f_{2,eq}) 2E_1 2E_2(\sigma_{1+2\to3+4}). \tag{5.22}$$

Next we need to separate the time dependence and energy dependence in the distribution functions. Full thermodynamic equilibrium involves both chemical equilibrium and kinetic equilibrium. Chemical equilibrium means that the number density matches that of the equilibrium value. Kinetic equilibrium on the other hand means that the distribution has the same energy dependence as the equilibrium value. We therefore separate the distribution function into two independent parts,

$$f(t, E, \mu) = g(t, \mu)h_{eq}(E). \tag{5.23}$$

Defining the `thermal average` of an operator $O_{i,j}$ as

$$\langle O_{i,j} \rangle = \int \frac{1}{n_{eq}^2} \frac{g_i d^3 p_i}{(2\pi)^3} \frac{g_j d^3 p_j}{(2\pi)^3} f_{i,eq} f_{2,eq} O_{i,j} \tag{5.24}$$

and denoting

$$v_{ij} = \left(\frac{(p_i p_j)^2 - m_i^2 m_j^2}{(p_i^2 + m_i^2)(p_j^2 + m_j^2)} \right)^{\frac{1}{2}} \tag{5.25}$$

lets us write the collision operator in a compact form

$$\hat{\mathbb{C}}_i = -(n_{DM}^2 - n_{eq}^2)\langle \sigma_{1+2 \Rightarrow 3+4} v \rangle. \tag{5.26}$$

Using this result we can write the time evolution of the number density

$$\frac{dn_{DM}}{dt} + 3Hn_{DM}t + (n_{DM}^2 - n_{eq}^2)\langle \sigma_{1+2 \Rightarrow 3+4} \rangle = 0 \tag{5.27}$$

which is the Lee-Weinberg equation that governs the freeze out process. In early stages, when the temperature is high $T \gg m_{S_{DM}}$ the collision term dominates. In this early era the number density will follow the equilibrium value. As the universe cools the collision term becomes less important as it becomes suppressed by the Boltzmann factors. The number density will follow the equilibrium value in the beginning but as the number density becomes increasingly suppressed the Hubble term takes over. Physically this means that the average time for a collision is of the order of the Hubble time.

In 5.1 this process is visualized as the blue lines. As the universe expands the temperature decreases and as the temperature goes below the mass of the dark matter particle the annihilation continue for a short while, resulting in the number density following the thermal equilibrium value. However in this era the collision term becomes increasingly suppressed by the Boltzmann factors until the dominant term in the time evolution of the number density is the Hubble term. The thermal equilibrium corresponds to the red lines that continue to decrease even after the dark matter has leveled off.

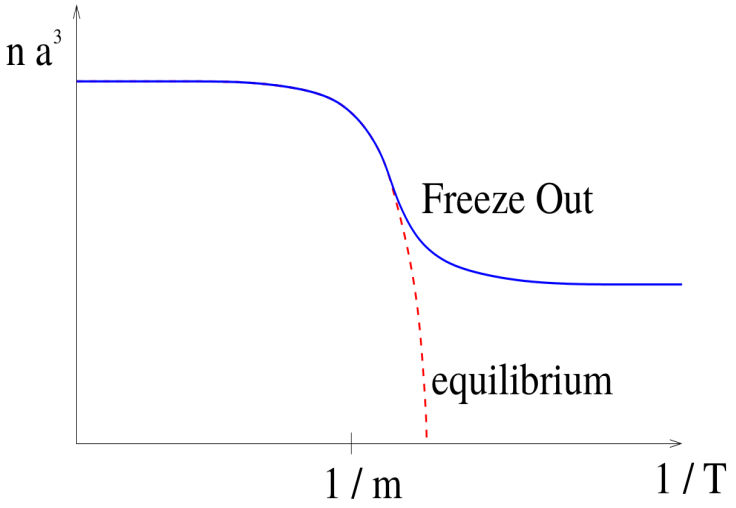

Figure 5.1: Thematic plot of the Freeze-out process [39]. On the y-axis is the number density times the expansion parameter cubed na^3 and on the x-axis the temperature. In blue is the number density for dark matter experiencing freeze-out. In red is shown the number density for a species in thermal equilibrium.

5.3 Relevant processes

In this section we briefly consider some processes for the dark matter annihilations. The relevant part in the annihilation processes are the dark matter-visible sector interactions. Since our dark matter candidate does not couple directly to the visible sector all interactions are mediated by the CP-even scalars h_1 and h_2. The CP-even scalars then couple to the matter sector as outlined in 3. Some of the contributing processes to the DM-singlet annihilation are shown in fig.5.2.

The amplitudes for the scalar annihilations can be calculated using the Feynman rules and the relevant parts for some of them are

$$A_{s-channel} \propto \frac{v_i Z_{1i}^H \lambda_i^{DM} \lambda_{h_i h_i h_j}}{(s - m_{h_i}^2) + i\Gamma_i m_{h_i}} \tag{5.28}$$

$$A_{t-channel} \propto \frac{\lambda_k^{DM} \lambda_l^{DM}}{t - m_{S_{DM}}^2} \tag{5.29}$$

$$A_{u-channel} \propto \frac{\lambda_m^{DM} \lambda_n^{DM}}{u - m_{S_{DM}}^2} \tag{5.30}$$

$$\tag{5.31}$$

and the couplings λ_i^{DM} are given by

$$\lambda_1^{DM} = \frac{m_{h_1}^2}{2v_s} \sin\theta \tag{5.32}$$

$$\lambda_2^{DM} = -\frac{m_{h_2}^2}{2v_s} \cos\theta. \tag{5.33}$$

The trilinear couplings $\lambda_{h_i h_i h_j}$ are given by the expressions 3.5 and 3.6. The Z^H_{kl} are elements of the rotation matrix Z^H and v_i is the VEV of the particle corresponding with which particle is represented twice in the coupling $\lambda_{h_i h_i h_j}$ in accordance with our parametrization of the trilinear couplings.

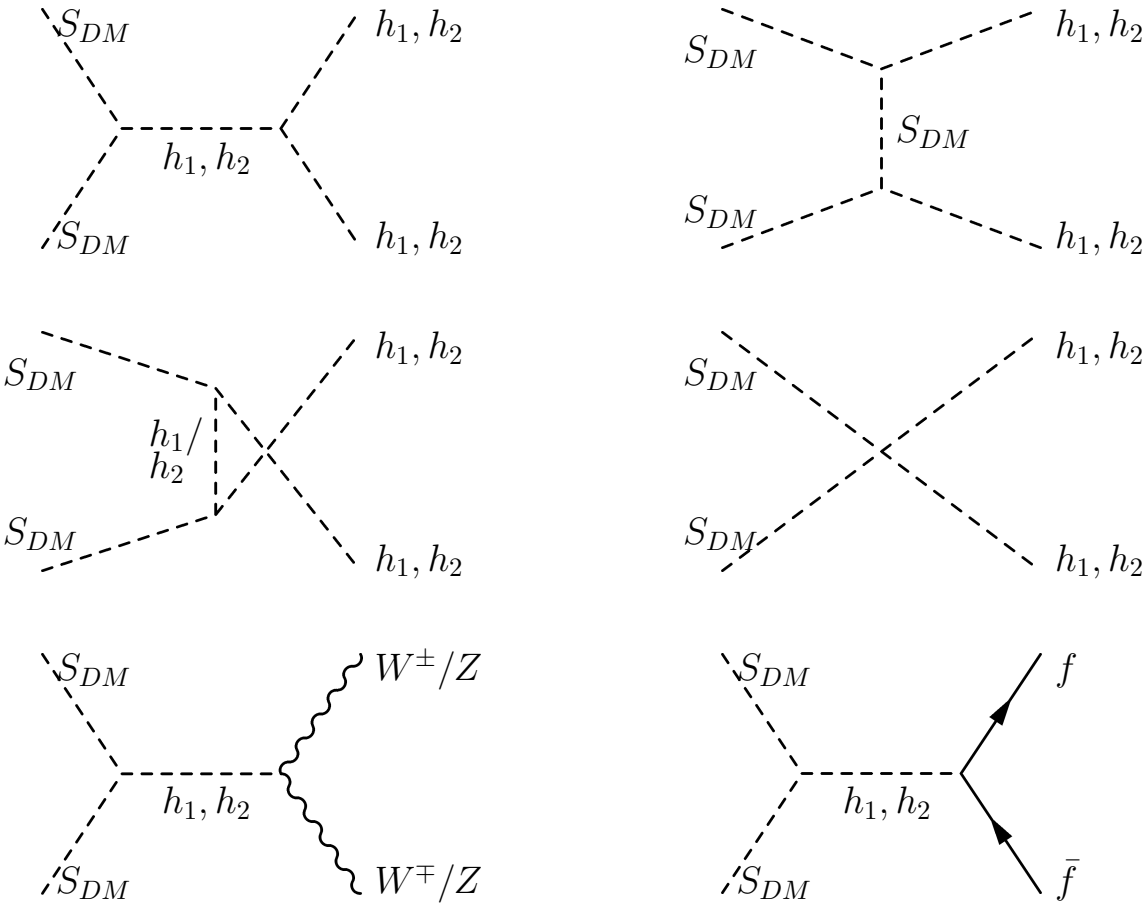

Figure 5.2: Some of the contributing Feynman diagrams to the processes $S_{DM}S_{DM} \to h_i h_i / \bar{f}f / VV$

From the amplitudes the matrix element squared for the annihilation process can be calculated. Since the entire expression is lengthy we will only consider select processes here. We need to take into account that we have three different outcomes, the DM particles can annihilate to $h_1 + h_1$,$h_2 + h_2$ or a combination of both h_1 and h_2. Neglecting to write every term separately we compactify by denoting the matrix element as

$$|M_{S^2_{DM} \to scalars}|^2 \propto \sum_{i,j} v_i^2 (Z^H_{1i})^2 \frac{(\lambda_i^{DM})^2 \lambda^2_{h_i h_i, h_j}}{(s - m_i^2)^2 + \Gamma_i^2 m_i^2} \tag{5.34}$$

but it should be understood that interference terms between the different scalars are not necessarily proportional to the same couplings and rotation matrix elements squared, i.e terms like $\sim \sin\theta \cos\theta$ arise as well. The cross section is easy to calculate since we have no spacial angular dependence in the matrix element. The cross section

is then proportional to

$$\sigma_{s-channel} \propto \frac{p_f^*}{16\pi s p_i^*} \sum_{i,j} \frac{v_i^2 (Z_{1i}^H)^2}{C_{i,i,j}^2} \frac{(\lambda_i^{DM})^2 \lambda_{h_i h_i, h_j}^2}{(s - m_i^2)^2 + \Gamma_i^2 m_i^2} \tag{5.35}$$

In the center of mass (CM) frame the 3-momenta of the dark matter particle can be rewritten using the triangle function

$$p^* = \frac{1}{2\sqrt{s}} \sqrt{\lambda(s, m_i, m_j)} \tag{5.36}$$

$$\lambda(s, m_i, m_j) = [s - (m_i - m_j)^2][s - (m_i + m_j)^2] = \frac{1}{2}\sqrt{s - m_{S_{DM}}^2} \tag{5.37}$$

since they have identical mass. For the final state particles the 3-momentum is given by

$$p^* = \frac{1}{2\sqrt{s}} \sqrt{[s - (m_i - m_j)^2][s - (m_i + m_j)^2]}. \tag{5.38}$$

In 5.35 we see that for off shell mediators the propagator has the form $1/(s - m_i^2)$, but as we approach the resonance the additional term in the propagator $m_i^2 \Gamma_i$ becomes significant. This resonance is referred to as the Breit-Wigner resonance where the cross section peaks sharply at the CM energy of the mediator particle.

The examples given in this section are only to illuminate some of the processes and their properties. The derivation of the complete annihilation cross section for the dark matter particle S_{DM} is beyond the scope of this thesis. To calculate the relic densities we will use computer packages that automate this process giving us opportunity to explore a wide variety of parameters.

5.4 Dark matter calculations and results

To confirm that the complex singlet extension can produce the required dark matter relic density we analyze the model with `SPheno`[6] and `micrOmegas`[7]. The model Lagrangian is first implemented in `SARAH`[5][40] which calculates loops and vertices. The output is then exported from `SARAH` to the `SPheno`-package. Using `SPheno` we can calculate particle spectrums and the masses in the scalar sector. With the spectrum file we can then calculate the relic density using `micrOmegas`.

We assume that the U(1) symmetry is gauged in the UV regime, i.e the theory considered is an effective field theory of a underlying local U(1) symmetric theory with a corresponding heavy gauge boson. This assumption is necessary to avoid the cosmological domain wall problem from the singlet VEV breaking the Z_2 symmetry[41].

We are not interested in a specific parameter combination but a range of values. It is therefore necessary to automate the scanning process which in our case was done with fortran code. The fortran code takes as input one or more parameter ranges and randomizes input values for the model in that range. These values are then

written to a LesHouches file that is then used as input when we compile `SPheno`. The `SPheno` output is exported to `micrOmegas` which is compiled using the values to obtain the relic density the parameter values would predict. Using this method a wide range of parameter values and combinations can be explored.

The output data is written to a file containing couplings, masses and dark matter relic density. This file is then analyzed using Python code. In the Python code the values are looped over to create plots in 2-D. For two of the scans we display the entire behavior $\Omega h^2 \in [0, 1]$ since they have more structure, but in general we only show the regions where $\Omega h^2 = 0.120 \pm 0.001$ since those parameter region are of interest since they comply with the PLANCK results [34]. We refer to this value for Ωh^2 as the correct relic density. The relic density for the full scans are shown as a copper color gradient in the range $\Omega h^2 \in [0, 1]$ for visualizing patterns in the parameter space. In appendix A.4 the extended parameter ranges are shown and are in general over a wider range of parameter values than the correct density plots shown in this chapter. The plots containing relic densities $\Omega h^2 = 0.120 \pm 0.001$ are shown using points in the parameter space. Plotting the relic density as a function of two parameters gives a better overview of how the relic density depends on input parameters. The h_1 mass has been kept fixed at $m_{h_1} \approx 125$GeV and the quartic coupling has not been varied. The white regions in the right plots of 5.4 and 5.5 corresponds to parameter combinations that are not allowed and in general produce negative $m_{h_2}^2$, or violate the $\lambda_1 \lambda_S > \lambda_{SH}^2$ condition.

Varied	Range 1	Range 2
$\lambda_{SH}, m_{S_{DM}}$	$\lambda_{SH} \in [0, 0.3]$	$m_{S_{DM}} \in [0, 50]$GeV
λ_{SH}, λ_S	$\lambda_{SH} \in [0, 0.06]$	$\lambda_S \in [0, 0.3]$
λ_S, v_s	$\lambda_S \in [0, 1]$	$v_s \in]0, 1500]$GeV
$m_{S_{DM}}, v_s$	$m_{S_{DM}} \in [0, 1500]$GeV	$v_s \in [0, 2500]$GeV
λ_{SH}, v_s	$\lambda_{SH} \in [0, 0.1]$	$m_{S_{DM}} \in [0, 1500]$GeV
$\lambda_S, m_{S_{DM}}$	$\lambda_S \in [0, 0.3]$	$m_{S_{DM}} \in [0, 250]$GeV

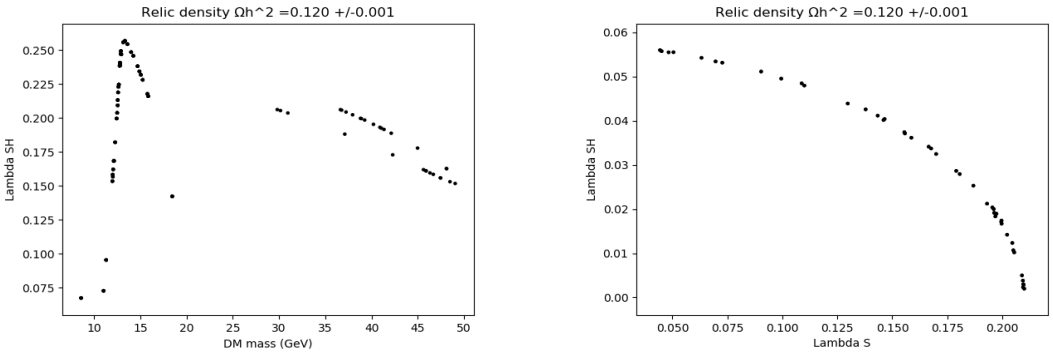

Figure 5.3: Left: Parameter combinations of $\lambda_{SH} \in [0, 0.3]$ and $m_{S_{DM}} \in [0, 50]$GeV resulting in correct relic density, $\Omega h^2 = 0.120 \pm 0.001$. Right: the parameter combinations $\lambda_S \in [0, 0.3]$ and $\lambda_{SH} \in [0, 0.06]$ that give the correct relic density.

In the first parameter scan, in the left of fig.5.3, for the case when the DM is

light $\mathcal{O}(10\text{GeV})$ the relic density is within experimental bounds. When we vary both couplings λ_S and λ_{SH} we first note that for some values we we violate the condition $\lambda_S\lambda_1 > \lambda_{SH}^2$. This is visualized with the white area to the left of the left graph A.2 bordering a sharp edge. This tells us that the parameter points beyond the edge are not calculated due to `SPheno` aborting the calculation because of a negative mass squared. When we then look at the correct relic density we see that the allowed region is a sector $\lambda_{SH}^2 + \lambda_S^2 \sim constant$. Also the preferred region is for low values of the coupling λ_{SH}.

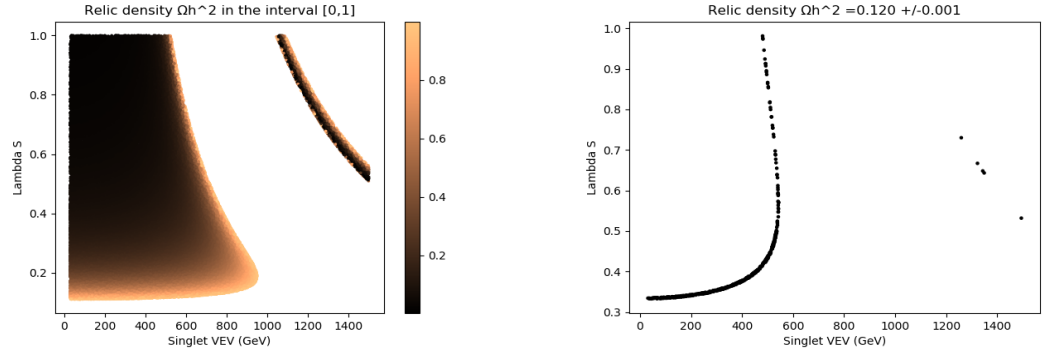

Figure 5.4: Left: The relic density as a function of $\lambda_S \in [0, 1]$ and $v_s \in]0, 1500]$GeV. The white regions corresponds to unphysical mass for the h_2 scalar or violate the condition $\lambda_1\lambda_S > \lambda_{SH}^2$. Right: The parameter combinations of λ_S and v_s that give the correct relic density.

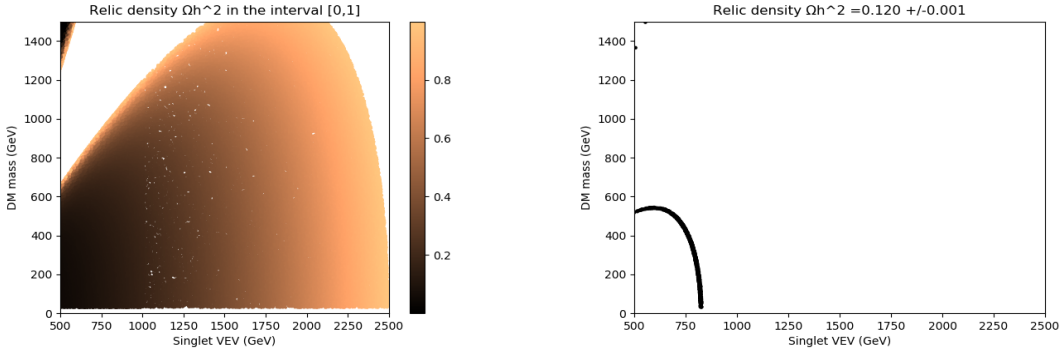

Figure 5.5: Left: Relic density variations under changes of $m_{S_{DM}} \in [0, 1500\text{GeV}]$ and $v_s \in [500, 2500]$GeV. The white regions have a unphysical mass for the h_2 scalar or violate the condition $\lambda_1\lambda_S > \lambda_{SH}^2$. Right: The points where the parameters give the correct relic density. The favoured region is close to the origin.

The next two scans scans have more interesting structure than the two previous ones. In the left figure of 5.4 we show relic densities in the interval $\Omega h^2 \in [0, 1]$. The white region in the left plot of 5.4 is a disallowed area where we have unphysical masses for the scalar h_2. The correct relic densities in the right plot of 5.4 does have a higher success rate near low v_s and λ_S, but some acceptable areas in higher VEV areas. The few successful parameter combinations in high VEV regions to the right are probably more abundant than the plot would entail. The scarce points are likely from a very narrow allowed region and since we are randomizing the parameters the probability of a hit in the narrow region is low.

The m_{DM}-v_s scan in fig.5.5 shows similar behavior as A.2 only in the opposite direction. Near the origin we find an acceptable region but we quickly overproduce dark matter as the parameters increase. This is expected since everything else being kept constant if the dark matter mass is larger the freeze-out occurs earlier since we reach the temperature $T \sim m_{S_{DM}}$ faster.

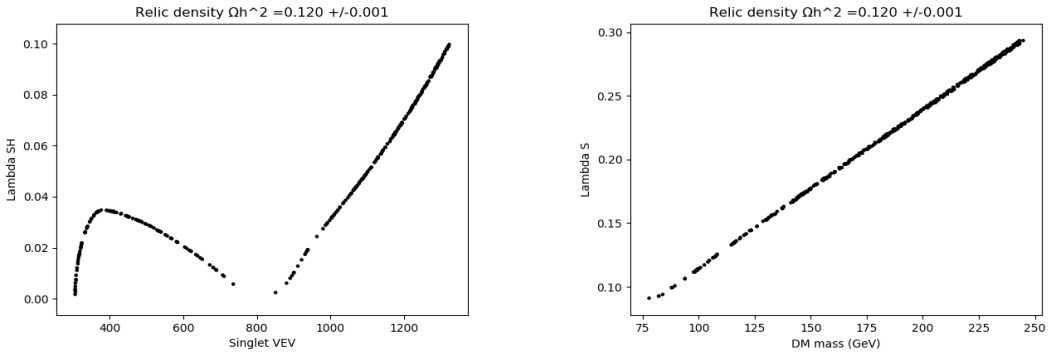

Figure 5.6: Left: Variations of $\lambda_{SH} \in [0, 0.1]$ and $v_s \in [0, 1300]$GeV giving the correct relic density. Right: The correct relic for variations of $\lambda_S \in [0, 0.3]$ and $m_{S_{DM}} \in [50, 250]$GeV.

Varying λ_{SH} and v_s does allow for a wide range of relic densities. The form of the left plot in 5.6 is not easily explained by elementary functions, but it does have a wide range of allowed regions as illustrated by the wider range scan shown in fig.A.5 of the appendix. At higher singlet VEVs the λ_{SH}-v_s dependence seems to be $\frac{\lambda_{SH}}{v_s} \sim constant$. This is very similar to the behavior of the right plot in 5.6 where the relationship appears to be linear, $\frac{m_{S_{DM}}}{\lambda_S} \sim constant$. This is also supported by the left side plot of A.6 which has a uniform gradient.

Further scans of the DM relic density can be found in [41]. These results require the DM relic density to be $\Omega h^2 = 0.1197 \pm 0.0022$. The h_1 mass is set to 125GeV and the mixing angle is set to $\sin\theta = 0.1$. In the left plot of 5.7 the second scalar mass is set to 300GeV. In the right plot the second scalar mass is 1TeV. The purple area is not allowed due to the Higgs decay to invisible constraint $Br(h_1 \to invisible) \leq 0.11$ at a 95% confidence level. The grey area is the unitarity limit where perturbation calculations break down. The dips correspond to the resonant annihilations $m_{h_1}/2$ and $m_{h_2}/2$.

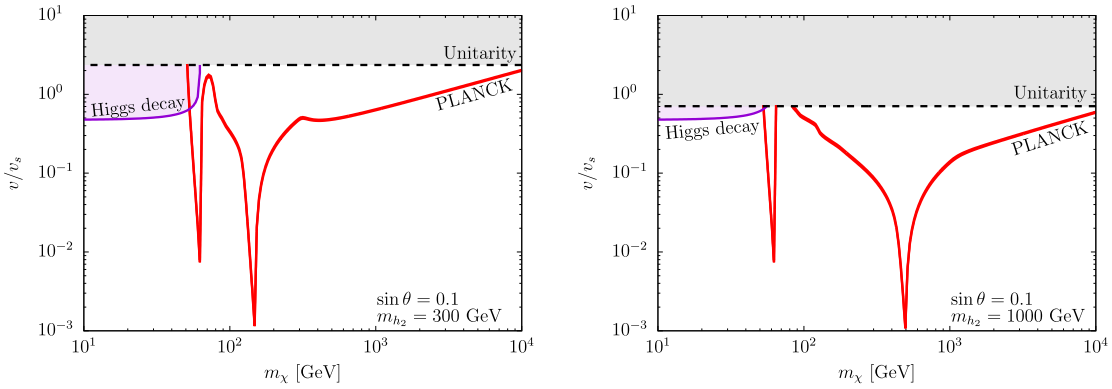

Figure 5.7: The parameter regions that give the correct relic density (red band). Left: $m_{h_2} =$ 300GeV. Right: $m_{h_2} = 1$TeV

The main annihilation channels are

Mass range of the DM	Main annihilation channels
$m_{S_{DM}} \leq m_W$	$S_{DM}S_{DM} \to \hat{b}\hat{b}; \hat{c}c$
$m_W \leq m_{S_{DM}} \leq m_{h_2}$	$S_{DM}S_{DM} \to WW; ZZ; h_1h_1$
$m_{h_2} \leq m_{S_{DM}}$	$S_{DM}S_{DM} \to h_2h_2$

In [41] the authors concluded that at tree level the direct detection cross section is suppressed as also discussed in 3. At loop order this cancellation is obviously spoiled but the effect is suppressed. By setting the loop functions to one one can estimate the dark matter-nucleon cross section

$$\sigma_{S_{DM}N} \sim \frac{\sin^2\theta}{64\pi^5} \frac{m_N^4 m_{h_2}^8 f_N^2}{v^2 v_s^6 m_{h_1}^4 m_{S_{DM}}^2} \tag{5.39}$$

with the nucleon mass m_N and $f_N \approx 0.3$ parametrizes the h_1-nucleon coupling. The cross section is $\sigma \sim 10^{-49} cm^2$ for $\sin\theta = 0.1$ and $m_{h_2} = 300$GeV. The DM mass is $m_{S_{DM}} \sim 1$TeV. The most stringent XENON1T constraint is $\sigma_{min} \approx 10^{-46}\text{cm}^2$[42] which is still orders of magnitude larger than the cross section in 5.39. In the limit $m_{S_{DM}} \to 0$ the broken $U(1)$ symmetry is restored, and the loop corrections vanish. This has the consequence that for light dark matter the cross section is suppressed by $m_{S_{DM}}^4/m_{h_2}^4$.

5.5 Summary of pseudo-Goldstone dark matter

One of the main arguments for the complex singlet model is to account for dark matter. With a softly broken $U(1)$ symmetry we can give mass to the CP-odd part of the singlet which then becomes a promising dark matter candidate. The broken symmetry needs to be gauged at some energy level to avoid cosmological domain walls.

The relic density is governed by the Boltzmann equation relating the number density of a particle to the expansion of the universe. This equation has been

implemented in computer packages to calculate dark matter relic densities. Using a combination of computer packages the evaluation of a wide range of parameters of the model was performed to give a glimpse of how dark matter relic density reacts to variations of different parameter combinations.

Using fortran and Python code a wide range of parameters have been explored and plotted to aid in the search for an optimal parameter range satisfying all constraints. The complex singlet has plenty of parameter regions satisfying the constraints on dark matter relic density set by PLANCK. Further the direct detection cross section of the dark matter particle scattering on nuclei $\sigma_{S_{DM}N} \sim \mathcal{O}(10^{-49} cm^2)$ is orders of magnitude smaller than even the most stringent XENON1T bounds of $\sigma \sim \mathcal{O}(10^{-42} cm^2)$ for light DM. The direct detection cross section is suppressed by a cancellation in the amplitude for small exchanged momenta.

6. EW vacuum stability

Before the discovery of the Higgs the stability of the electroweak vacuum was an open question[43]. This is because the loop corrections to the quartic coupling in the Higgs potential are negative for high energies. This would imply that the vacuum of the Higgs potential has a second (or multiple, depending on beyond the standard model physics) lower energy minimum. This scenario would be considered the metastable case, where the current vacuum is long lived but not stable. The instability depends on the Higgs mass, the top mass (primarily) and the strong coupling[44].

The couplings in quantum field theories run with energy scale. In the Higgs case the coupling gets corrections from all quarks due to the Yukawa coupling. The biggest correction comes from loops involving the top quark, due to its high mass $m_t \sim 172\text{GeV}$[45].

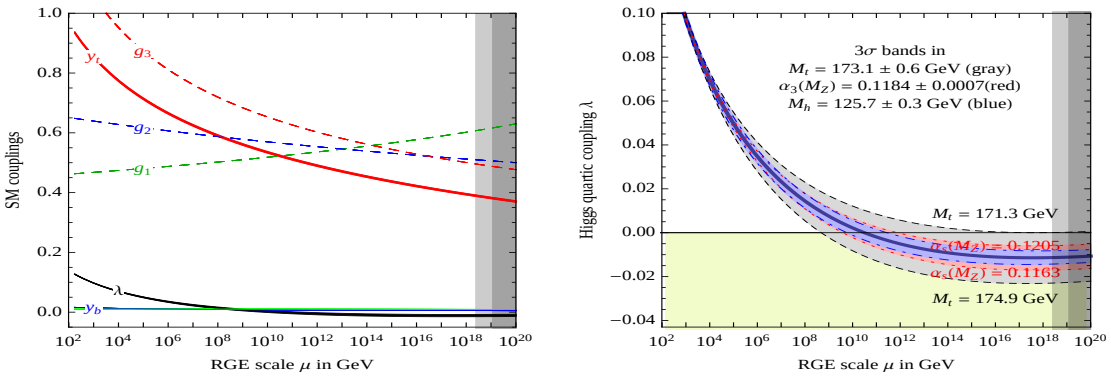

Figure 6.1: Left: The running of couplings in the SM at NNLO. Right: The Higgs quartic coupling dependence on the top mass. G. Degrassi et al.

The right figure of 6.1 shows that the Higgs quartic coupling turns negative at $E \sim 10^{11}\text{GeV}$. This would imply the electroweak vacuum is metastable. Whether it actually is metastable or stabilized by some undiscovered particle is still an open question. In the left plot of 6.1 the running of Standard Model couplings is shown.

In this chapter we will discuss the necessary formalism to solve renormalization group equations, that govern the couplings energy dependence. We will then use this methodology to calculate the contributions to the SM like Higgs quartic coupling using `SARAH` in order to see if the singlet extension can stabilize the electroweak potential up to Planck scale.

6.1 Renormalization group flow

Any quantum field theory process is a sum of infinitely many terms in the perturbation theory. Some of the terms involve internal loops that diverge at high energies/small distances. These divergences need to be cancelled since they would lead to unphysical predictions. Take for example one of the photon propagator loop corrections which has a

$$\propto \int d^4k \frac{1}{k^2 - m_f^2} \tag{6.1}$$

term at one loop order. This term corresponds to the rightmost Feynman diagram in 6.2, and diverges as $\sim k^2$ at large momentum.

Figure 6.2: The schematic expansion of the photon propagator.

To avoid these UV-divergences, counterterms need to be introduced to cancel the divergent parts. This process is known as the renormalization of a theory[46]. The renormalization procedure involves introducing a finite number of counterterms to cancel all divergences.

Evidently if we integrate 6.1 up to some cutoff Λ the theory is finite but depends on the cutoff. Calculating diagrams using the bare mass m_0 and the bare coupling λ_0 and using the cutoff Λ makes the theory cutoff dependent. In the calculations of matrix elements one also takes into account how the field strength scales with the cutoff. One can then combine all these expressions to eliminate the bare quantities to make the amplitude finite even if the cutoff limit $\Lambda \to \infty$[47]. This process is the renormalization procedure. By rewriting the bare quantities m_0 and λ_0 into the cutoff dependent parameters $m(\Lambda)$ and $\lambda(\Lambda)$ the matrix element is finite at all cutoff scales.

Now we need to introduce mathematical rigour to this process. We will follow closely the derivation in Peskin & Schroeder, "An Introduction to Quantum Field Theory"[47]. Consider a generic real ϕ^4-theory in Euclidean space with the Lagrangian

$$\mathcal{L} = \frac{1}{2}(\partial_\mu \phi)(\partial^\mu \phi) + \frac{1}{2}m^2\phi^2 + \frac{\lambda}{4!}\phi^4 \tag{6.2}$$

The generating functional (without external sources) is then

$$\mathcal{Z} = \int \prod_k d\phi(k) \exp\left[- \int d^dx \left(\frac{1}{2}(\partial_\mu \phi)(\partial^\mu \phi) + \frac{1}{2}m^2\phi^2 + \frac{\lambda}{4!}\phi^4 \right) \right] \tag{6.3}$$

Next we separate the integration degrees of freedom in two groups. Take a fraction $b \in [0,1]$ of some high momentum Λ, i.e $b\Lambda$. Then we call momentum in the range $b\Lambda \leq |k| < \Lambda$ the high momentum degrees of freedom that we relabel to

$$\hat{\phi}(k) = \begin{cases} \phi(k) & \text{when } b\Lambda \leq |k| < \Lambda; \\ 0 & \text{otherwise.} \end{cases} \tag{6.4}$$

We also define

$$\phi(k) = \begin{cases} \phi(k) & \text{when } |k| < b\Lambda; \\ 0 & \text{otherwise.} \end{cases} \tag{6.5}$$

i.e $\phi(k)$ is identical to the old one for $|k| < b\Lambda$. Rewriting then the generating functional using these redefinitions to

$$\mathcal{Z} = \int \prod_k d\phi(k) \int \prod_k d\hat{\phi}(k) \exp\Big[- \int d^d x \left(\frac{1}{2}(\partial_\mu \phi + \partial_\mu \hat{\phi})^2 \right. \tag{6.6}$$

$$\left. + \frac{1}{2} m^2 (\phi + \hat{\phi})^2 + \frac{\lambda}{4!}(\phi + \hat{\phi})^4 \right) \Big] \tag{6.7}$$

and now we need to open up the parenthesis. Fourier components of different wavelengths are orthogonal so any combination $\sim \phi\hat{\phi}$ is zero. The generating functional is then of the form

$$\mathcal{Z} = \int \mathcal{D}\phi(k) \exp\left[- \int d^d x \left(\frac{1}{2} \partial_\mu \phi \partial^\mu \phi + \frac{1}{2} m^2 \phi^2 + \frac{\lambda}{4!} \phi^4 \right) \right] \tag{6.8}$$

$$\int \mathcal{D}\hat{\phi}(k) \exp\left[- \int d^d x \left(\frac{1}{2}(\partial_\mu \hat{\phi})^2 + \frac{1}{2} m^2 \hat{\phi}^2 + \lambda \left[\frac{1}{6}\phi^3 \hat{\phi} + \frac{1}{4}\phi^2 \hat{\phi}^2 + \frac{1}{6}\phi \hat{\phi}^3 + \frac{1}{4!}\hat{\phi}^4 \right] \right) \right] \tag{6.9}$$

and we can shorten the first Lagrangian to just $\mathcal{L}_0(\phi)$ for convenience. Next we treat everything apart from the derivative term as a perturbation. This includes the mass term since we assume $\Lambda^2 \gg m^2$. The space-time integral can be rewritten in terms of Fourier coefficients

$$\int d^d x \frac{1}{2}(\partial_\mu \phi)^2 = \sum_n \frac{1}{2V} k_n^2 \phi^*(k_n) \phi(k_n). \tag{6.10}$$

where V is the integration volume. Taking the functional derivative of the generating functional gives the correlation functions. For the two point function the expression is

$$\overline{\phi(p)\phi(k)} = \frac{1}{Z_0} \left(-i \frac{\delta}{\delta J(p)} \right) \left(-i \frac{\delta}{\delta J(k)} \right) Z[0] \Big|_{J=0} \tag{6.11}$$

and in our case $Z_0 = Z[J]$ since $J = 0$. This leads to the expression for the two point correlator for eq.6.9 which is given by

$$\overline{\hat{\phi}(p)\hat{\phi}(k)} = \frac{\int \mathcal{D}\hat{\phi} e^{-\int \mathcal{L}_0} \hat{\phi}(k)\hat{\phi}(p)}{\int \mathcal{D}\hat{\phi} e^{-\int \mathcal{L}_0}} = \frac{1}{k^2}(2\pi)^d \delta^d(k+p)\Theta(k) \tag{6.12}$$

with the step function $\Theta(k)$ defined by

$$\Theta(k) = \begin{cases} 1 & \text{when } b\Lambda \leq k \leq \Lambda; \\ 0 & \text{otherwise} \end{cases} \tag{6.13}$$

Turning now to the perturbations. All the perturbations (i.e the rest of the terms in 6.9) can be evaluated using Wick's theorem[47][48]. We can take the $\phi^2\hat{\phi}^2$ as an example. The result is

$$-\int d^dx \frac{\lambda}{4}\phi^2\overline{\hat{\phi}\hat{\phi}} = -\frac{1}{2}\int \frac{d^dk_1}{2\pi)^d}\frac{\lambda}{2}\int_{b\Lambda\leq k\leq\Lambda}\frac{d^dk}{(2\pi)^d}\frac{1}{k^2}\phi(k_1)\phi(-k_1) \tag{6.14}$$

since the propagator is 6.12. The second integral can be evaluated to

$$\int_{b\Lambda\leq k\leq\Lambda}\frac{d^dk}{(2\pi)^d}\frac{1}{k^2} = \frac{\lambda}{(4\pi)^{\frac{d}{2}}\Gamma\left(\frac{d}{2}\right)}\frac{1-b^{d-2}}{d-2}\Lambda^{d-2} \tag{6.15}$$

We can translate 6.14 to a diagrammatic representation. In this representation $\hat{\phi}^2$ corresponds to internal lines and ϕ^2 to external lines. Then 6.14 corresponds to 6.3

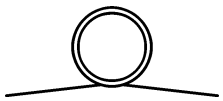

Figure 6.3: The $\hat{\phi}^2\phi^2$-term schematic representation

which does look like a loop correction to the mass term. At λ^2 order we have two contributing diagrams

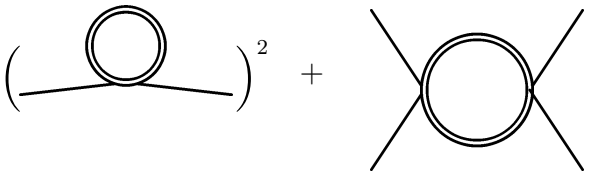

Figure 6.4: The two contributions at λ^2-order.

The first loop in 6.4 is a disconnected diagram that gives the $\mathcal{O}(\lambda^2)$ term to the perturbation. The second term is a new term that can be calculated to

$$= \frac{1}{4!}\int d^dx\ 4!\frac{2}{2!}\left(\frac{\lambda}{4}\right)^2\int_{b\Lambda\leq k\leq\Lambda}\frac{d^dk}{(2\pi)^d}\frac{1}{(k^2)^2}\phi^4 \tag{6.16}$$

and again we can evaluate the momentum integral obtaining the result

$$= \frac{1}{4!}\int d^d x \, \frac{3\lambda^2}{(4\pi)^{\frac{d}{2}}\Gamma\left(\frac{d}{2}\right)} \frac{(1-b^{d-4})}{d-4}\Lambda^{d-4} \tag{6.17}$$

for any dimension d. In the limit $d \to 4$ 6.17 reduces to

$$= \frac{1}{4!}\int d^d x \, \frac{3\lambda^2}{16\pi^2} \log\frac{1}{b} \tag{6.18}$$

which diverges as $b \to 0$, i.e as we integrate over the whole momentum space. In the expansion of 6.9 we also generate higher order ϕ terms than $\mathcal{O}(\phi^4)$. One such example is the $3 \to 3$ annihilation term

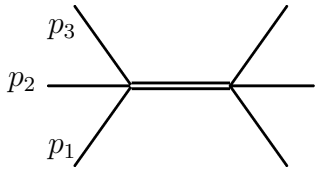

Figure 6.5: The diagram of the $1, 2, 3 \to a, b, c$ annihilation

which gives a contribution

$$\propto \frac{\lambda^2}{(p_1+p_2+p_3)^2}\Theta(p_1+p_2+p_3) \tag{6.19}$$

for the incoming momenta p_i. Summing all diagrams is equal to the exponent of the sum of all connected diagrams[47]

$$\sum(\text{diagrams}) = e^{\sum(\text{connected diagrams})}. \tag{6.20}$$

With this the effective Lagrangian $\mathcal{L}_{eff}$ is finally

$$\mathcal{L}_{eff} = \frac{1}{2}\partial_\mu\phi\partial^\mu\phi + \frac{1}{2}m^2\phi^2\frac{1}{4!}\lambda\phi^4 + \text{sum of all connected diagrams} \tag{6.21}$$

that we will use to understand renormalization and renormalization group flows. We also introduce corrections from diagrams as $\Delta\mathcal{O}$ for the terms in the Lagrangian giving

$$\mathcal{L}_{eff} = \int d^d x \left(\frac{1}{2}(1+\Delta Z)(\partial_\mu\phi\partial^\mu\phi) + \frac{1}{2}(m^2+\Delta m^2)\phi^2 + \frac{1}{4!}(\lambda+\Delta\lambda)\phi^4 \right. \tag{6.22}$$

$$\left. \Delta C(\partial_\mu\phi\partial^\mu\phi)^2 + \Delta D\phi^6 + \text{etc}\ldots\right). \tag{6.23}$$

Next we rescale distances and momentum as

$$k^{'} = \frac{k}{b} \tag{6.24}$$

$$x^{'} = xb \tag{6.25}$$

which means that the momentum $k^{'}$ is integrated over when $k^{'} < \Lambda$. Recalculating $\mathcal{L}_{eff}$ with the rescaled coordinates and momenta gives

$$\mathcal{L}_{eff} = \int d^d x'\ b^{-d} \left(\frac{1}{2}(1+\Delta Z) b^2 (\partial^{'}_{\mu}\phi \partial^{\mu'}\phi) + \frac{1}{2}(m^2 + \Delta m^2)\phi^2 + \frac{1}{4!}(\lambda + \Delta\lambda)\phi^4 \right. \tag{6.26}$$

$$\left. b^4 \Delta C (\partial^{'}_{\mu}\phi \partial^{\mu'}\phi)^2 + \Delta D \phi^6 + \text{etc}\ldots \right), \tag{6.27}$$

assuming b is not position dependent. From 6.9 and 6.12 we can see that we get the same propagator if we rescale the field as

$$\phi' = \sqrt{b^{2-d}(1+\Delta Z)}\ \phi \tag{6.28}$$

This transforms the effective Lagrangian to

$$\mathcal{L}_{eff} = \int d^d x'\ \left(\frac{1}{2}(\partial'_{\mu}\phi' \partial'^{\mu}\phi') + \frac{1}{2} m'^2 \phi'^2 + \frac{1}{4!}\lambda' \phi'^4 \right. \tag{6.29}$$

$$\left. C'(\partial'_{\mu}\phi' \partial'^{\mu}\phi')^2 + D' \phi'^6 + \text{etc}\ldots \right). \tag{6.30}$$

with the new masses and couplings

$$m'^2 = (m^2 + \Delta m^2)(1+\Delta Z)^{-1} b^{-2} \tag{6.31}$$

$$\lambda' = (\lambda + \Delta\lambda)(1+\Delta Z)^{-2} b^{d-4} \tag{6.32}$$

$$C' = (C + \Delta C)(1+\Delta Z)^{-2} b^{d} \tag{6.33}$$

$$D' = (D + \Delta D)(1+\Delta Z)^{-3} b^{2d-6} \tag{6.34}$$

In the limit when $b \sim 1$ the shells of momentum space tend to 0 making the transformation above continuous. In the continuous limit this procedure of rescaling and integrating out high momentum degrees of freedom can be described as a flow in the space of possible Lagrangians. This flow is called the renormalization group. Take the shifted parameters in 6.31 - 6.34 and consider them close to the stationary point of

$$\mathcal{L}_{eff} = \frac{1}{2}\partial_{\mu}\phi \partial^{\mu}\phi \tag{6.35}$$

when all perturbations in 6.8 and 6.9 are zero. The shift in 6.31 - 6.34 to leading order is then

$$m'^2 \simeq m^2 b^{-2},\ \lambda' \simeq \lambda b^{d-4},\ C' \simeq C b^d,\ D' \simeq D b^{2d-6} \tag{6.36}$$

showing the scaling of the parameters close to the point we defined as stationary by 6.28 and 6.29

6.2 Callan-Symanzik Equation and RGE

From the generating functional in the previous section we now focus on the propagator. We defined the propagator for a massless ϕ^4-theory in 6.12 when $k^2 = 0$. Now we consider the propagator at some arbitrary scale $k^2 = -M^2$. This means that instead of the propagator having a coefficient of 1 at $k^2 = 0$ it instead occurs at some arbitrary momentum $k^2 = -M^2$. In diagram form this is

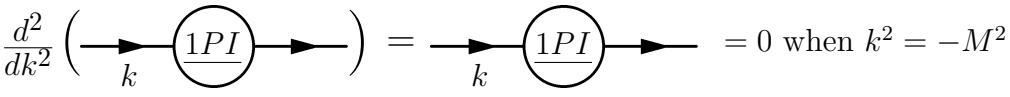

Figure 6.6: The renormalization level matching condition $k^2 = -M^2$ for the pole (left) and propagator (right)

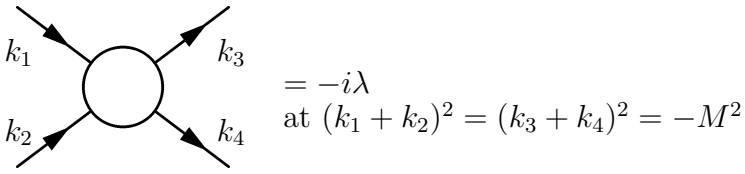

Figure 6.7: The renormalization level matching condition for the quartic coupling when $k^2 = -M^2$ in the massless ϕ^4-theory.

defining our renormalized field at the scale $k^2 = -M^2$. This renormalized field is related to the bare field [1] by the scale factor Z;

$$\phi = Z^{-\frac{1}{2}}\phi_0 \tag{6.37}$$

meaning in terms of bare fields ϕ_0, the renormalized propagator is

$$\langle\Omega|\,\phi_0(k)\phi_0(-k)\,|\Omega\rangle = \frac{iZ}{k^2},\ \text{at } k^2 = -M^2. \tag{6.38}$$

The counterterms that need to be introduced to maintain physical observables are related to the field rescaling Z as

$$\delta_Z = Z - 1 \tag{6.39}$$

but the counterterms now need to be readjusted to comply with the new conditions 6.6 and 6.7. The n-point Greens functions in a renormalized theory is

$$G^n(x_1, x_2, ...x_n) = \langle\Omega|\,\mathcal{T}\phi(x_1)\phi(x_2)...\phi(x_n)\,|\Omega\rangle_{connected} \tag{6.40}$$

where $\mathcal{T}$ is the time ordering operator. If we now shift the renormalization scale by a small amount δM we demand that the bare field Greens functions are invariant

[1] The bare field is the original field written in terms of bare couplings and masses, i.e before renormalization

since the bare Greens functions have no M-dependence. This shift in scale induces shifts in all parameters of the theory

$$M \to M + \delta M \tag{6.41}$$
$$\lambda \to \lambda + \delta\lambda \tag{6.42}$$
$$\phi = Z\phi_0 \to Z'\phi = (1 + \delta\eta)\phi \tag{6.43}$$

and then the renormalized Greens functions shifts as

$$G^n \to (1 + n\delta\eta)G^n. \tag{6.44}$$

This transformation can then be written as

$$\frac{dG^n}{dM} = \frac{\partial G^n}{\partial M}\delta M + \frac{\partial G^n}{\partial \lambda}\delta\lambda = n\delta\eta G^n. \tag{6.45}$$

If we consider the n-point Greens function as a function of M and δ. Making the substitutions

$$\beta \equiv \frac{M}{\delta M}\delta\lambda, \quad \gamma \equiv -\frac{M}{\delta M}\delta\eta \tag{6.46}$$

we write 6.45 in the form

$$\left[M\frac{\partial}{\partial M} + \beta\frac{\partial}{\partial\lambda} + n\gamma\right] G^n(x_1, x_2, ...x_n) \tag{6.47}$$

and since the Greens function is the renormalized Greens function, β and γ cannot depend on M and they can only be functions of λ. This means that for our massless ϕ^4 theory the renormalized Greens function must satisfy

$$\left[M\frac{\partial}{\partial M} + \beta(\lambda)\frac{\partial}{\partial\lambda} + n\gamma(\lambda)\right] G^n(x_1, x_2, ...x_n) = 0 \tag{6.48}$$

which is the Callan-Symanzik equation for massless ϕ^4-theory that tells us there are two functions β and γ that compensate any shift in renormalization scale.

6.3 Complex singlet β-functions

The Callan-Symanzik equation tells us how the coupling and the field itself scales under shifts of renormalization scale. The $\gamma(\lambda)$ function is called the anomalous dimension and relates renormalization scale to the field scaling. The β-function tells us how the couplings scale with changes in renormalization scale.

From these β-functions one can solve the couplings dependence on energy scale, the so called running of the coupling that we referred to in the beginning of this chapter and is plotted to the left of 6.1. Take for example the one-loop β function of a massless ϕ^4-theory

$$\mathcal{L}_{\phi^4} = \frac{1}{2}\partial_\mu\phi\partial^\mu\phi - \frac{1}{2}m_0^2\phi^2 - \frac{1}{4!}\lambda_0\phi^4. \tag{6.49}$$

with the β-function given by

$$\beta(\lambda) = \frac{3\lambda^2}{16\pi^2} + \mathcal{O}(\lambda^3) \tag{6.50}$$

From the definition of the β-function[49],

$$\beta(\bar{\lambda}) \equiv \frac{d}{d\log\left(\frac{k}{M}\right)}\bar{\lambda}(k,\lambda) \tag{6.51}$$

we can solve the running coupling $\bar{\lambda}$ as a function of energy scale

$$\bar{\lambda}(k) = \frac{\lambda_0}{1 - \frac{3\lambda_0}{16\pi^2}\log\frac{k}{M}} \tag{6.52}$$

with the bare coupling given by λ_0. Clearly when $p = M$ the running coupling is given by $\bar{\lambda} = \lambda_0$ i.e the scale where we defined our renormalized theory. The β functions therefore describe the rate of renormalization group flow of the couplings.

The β-functions for the complex singlet extension are calculated with `SARAH`[5]. This is done by implementing the complex extension in a `model.m`-file. The potential is given by 2.4. The calculations of the β-functions in `SARAH` are done by the command `CalcRGEs[]`. The result is then written to a LaTeX-file and also saved separately in `Mathematica`. The β-functions as calculated by `SARAH` are displayed in their entirety in the appendix A.3. The Higgs quartic coupling λ_1 one loop β function is calculated to

$$\beta_{\lambda_1} = -\frac{9}{5}g_1^2\lambda_1 - 9g_2^2\lambda_1 + 12\lambda_1^2 + 2\lambda_{SH}^2 + 12\lambda_1\mathrm{Tr}|Y_d|^2 + 4\lambda_1\mathrm{Tr}|Y_e|^2 \tag{6.53}$$

$$+ 12\lambda_1\mathrm{Tr}|Y_u|^2 - 12\mathrm{Tr}|Y_d|^4 - 4\mathrm{Tr}|Y_e|^4 - 12\mathrm{Tr}|Y_u|^4 \tag{6.54}$$

in the complex singlet extension. The traces are over the Standard Model like Yukawa coupling matrices. The additional term $2\lambda_{SH}^2$ can then be used to lift the electroweak vacuum to be completely stable. `SARAH` is capable of calculating β-functions to two loop level. We can then use the two loop β-functions to see if the λ_{SH}-coupling can stabilize the electroweak vacuum at Next-to-Next-to-Leading order (NNLO). The additional terms in the two loop β-functions, when compared to the Standard Model, are

$$\beta \sim -10\lambda_1\lambda_{SH}^2 \pm 8\lambda_{SH}^3 \tag{6.55}$$

the signs corresponding to the sign of the portal coupling in the potential 2.4. Solving and plotting the running of the couplings can be done in `Mathematica`. The initial values are $\lambda_1 = 0.27$, $g'(m_t) = 0.35 = \sqrt{3/5}\ g_1$, $g(m_t) = 0.64 = g_2$ and $g_s(m_t) = 1.16 = g_3$. The top-Yukawa is taken to be $Y_t = 0.93$[50] at the top mass. We ignore the rest of the quarks and leptons since their contribution is negligible.

We see in 6.8 that it is possible to have a positive-definite quartic coupling λ_1 even up to the Planck scale $m_P = 2.4 \times 10^{18}$GeV, with both positive (left) and negative (right) sign of λ_{SH}. At high couplings $\lambda_{SH} \gtrsim 0.26$ the perturbativity puts the constraints due to the positive contribution of λ_{SH} in both $\beta_{\lambda_{SH}}$ and β_{λ_S}[11].

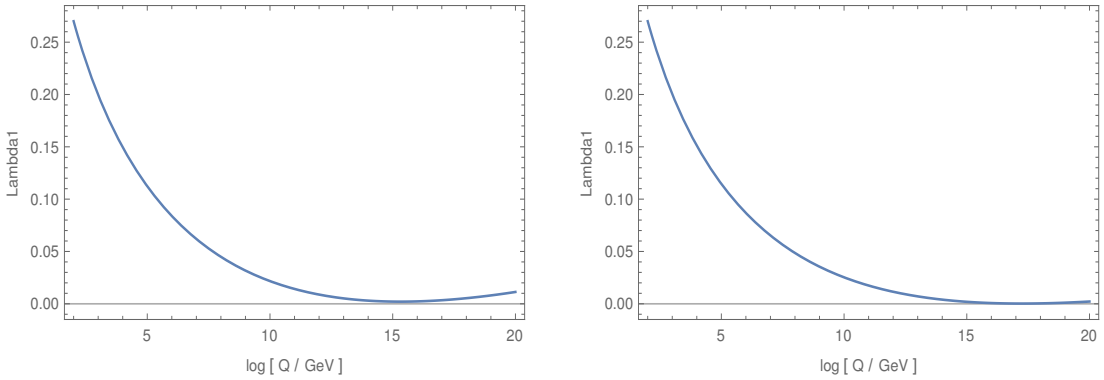

Figure 6.8: The running of the Higgs quartic coupling with positive sign (left) and negative (right) of λ_{SH}, the portal coupling has the value $\lambda_{SH} = 0.22$ and $\lambda_{SH} = 0.27$ respectively.

6.4 Summary

One of the main motivations for the complex singlet extension was the prospect of stabilizing the electroweak vacuum with minimal additions to the Standard model. This effect is competing with dark matter production since both depend on the λ_{SH} coupling, albeit in different ways. The electroweak vacuum stability favors a larger coupling and therefore puts constraints on the other Lagrangian parameters if the correct relic density is to be produced.

By solving the expression for the coupling in 3.3 we can put a limit on the scalar mass difference mass and the VEV v_s. If we use the conservative limit of $\sin\theta = 0.15$ the limit is given by

$$\frac{1}{v_s}(m_{h_2}^2 - m_{h_1}^2) > 432\text{GeV} \tag{6.56}$$

and assuming $m_{h_1}^2/v_s \ll m_{h_2}^2/v_s$ the limit simplifies to

$$\frac{m_{h_2}^2}{v_s} \gtrsim 432\text{GeV}. \tag{6.57}$$

We see in 6.57 that the conservative limit on the mixing angle θ is justified since this requires the h_2 mass to be of order of magnitude greater than its VEV.

7. Conclusions

We have studied the complex singlet scalar extension of the Standard model in a softly broken $U(1)$ symmetric model. The two CP-even states mix to form mass eigenstates. The resulting massive pseudo-Goldstone boson in the model is a viable dark matter candidate. We have explored direct and indirect detection prospects of the dark matter candidate, and the possible collider signatures of the model.

The models predictions were compared to particle physics experiments since some measurements, especially in the electroweak sector, are very accurate and constrain allowed parameter values. We also considered the searches for the Higgs boson. These were Higgs coupling measurements and direct Higgs searches. In the mass range $1\text{GeV} < m_{h_2} < 450\text{GeV}$, the direct Higgs boson searches and coupling measurements were the limiting experiments variably constraining the mixing angle to $\sin\theta \lesssim 0.2 - 0.4$ depending on the h_2 mass.

At high masses $m_{h_2} > 450\text{GeV}$ the electroweak measurements provide the most stringent bounds. By introducing a second scalar that mixes with the Standard model like Higgs we have new loop contributions to gauge boson processes. The predictions were compared to measured values to constrain the model further. The limit on the mixing angle from EWPO was found to be $\sin\theta \sim 0.3$, monotonically decreasing as the h_2 mass increases. We also calculated the Peskin-Takeuchi parameters S and T in the limit $m_{h_1} \ll m_{h_2}$. We found that the mixing angle must be $|\sin\theta| < 0.15$ for this heavy scalar to comply with measurements.

In the dark matter section of the thesis we derived the Boltzmann equation in an expanding universe and then applied the equation in the computer package `micrOmegas`. By randomly generating parameter points while keeping every other parameter fixed we showed how different parameter combinations influence the relic density of S_{DM}. The relic density varied greatly depending on the parameters chosen, and in general only small regions of parameters were acceptable if one assumes the relic density of S_{DM} must account for all dark matter observed today, $\Omega h^2 = 0.120 \pm 0.001$.

The parameter space of the model is further constrained by stability requirements of the electroweak vacuum. For this, we derived the β-functions for the coupling parameters by generating functionals to obtain the Callan-Symanzik equation to study the running of the couplings. For the electroweak to be stable, one requires for the Higgs quartic coupling λ_1 to be positive definite. For this condition to be satisfied up to the Planck scale, we showed that the portal coupling should have a value of at least $\lambda_{SH} \approx 0.26$ at the electroweak scale when λ_1 and λ_{SH} have the same sign. If the portal coupling and Higgs quartic coupling have a relative sign

difference, the portal coupling at electroweak scale must be at least $\lambda_{SH} = 0.28$ to have a stable vacuum, as our calculations show.

In conclusion, the complex singlet scalar extension of the Standard Model is an economic framework which could explain some of the shortcomings of the Standard Model. Among these are providing a viable dark matter candidate and stability of the electroweak vacuum up to the Planck scale. Future collider experiments, including the upgraded LHC, might result in better measurements of the Higgs quartic coupling and the top quark mass. It is therefore motivated to make a more robust analysis with updated constraints on the model in future.

A. Appendices

A.1 The Lagrangian

Below the Lagrangian is displayed as written in the SARAH implementation.

$$\begin{aligned}
V_{int} =& -\frac{1}{4}\mu_S'^2 S^2 - \frac{1}{2}\mu^2|H^0|^2 - \frac{1}{2}\mu^2|H^+|^2 - \frac{1}{2}M_S^2|S|^2 \\
& - \frac{1}{2}\lambda_1|H^0|^4 - \frac{1}{2}\lambda_1|H^+|^4 - \frac{1}{2}\lambda_S|S|^4 - H^+\lambda_1|H^0|^2H^- \\
& - \lambda_{SH}|S|^2|H^0|^2 - \lambda_{SH}|S|^2|H^+|^2 - \frac{1}{4}\mu_S'^2 S^{*2} \\
& - H^0 d^*_{L,k\gamma}Y^*_{d,jk}\delta_{\beta\gamma}d_{R,j\beta} - H^+u^*_{L,k\gamma}Y^*_{d,jk}\delta_{\beta\gamma}d_{R,j\beta} \\
& - H^0 e^*_{L,k}Y^*_{e,jk}e_{R,j} - H^+\nu^*_{L,k}Y^*_{e,jk}e_{R,j} - H^-d^*_{L,k\gamma}Y^*_{u,jk}\delta_{\beta\gamma}u_{R,j\beta} \\
& + H^{0,*}u^*_{L,k\gamma}Y^*_{u,jk}\delta_{\beta\gamma}u_{R,j\beta} - H^{0,*}d^*_{R,j\beta}\delta_{\beta\gamma}d_{L,k\gamma}Y_{d,jk} \\
& - H^{0,*}e^*_{R,j}e_{L,k}Y_{e,jk} - H^-e^*_{R,j}\nu_{L,k}Y_{e,jk} - H^+u^*_{R,j\beta}\delta_{\beta\gamma}d_{L,k\gamma}Y_{u,jk} \\
& - H^-d^*_{R,j\beta}\delta_{\beta\gamma}u_{L,k\gamma}Y_{d,jk} + H^0u^*_{R,j\beta}\delta_{\beta\gamma}u_{L,k\gamma}Y_{u,jk}
\end{aligned} \tag{A.1}$$

A.2 The detailed derivation of the couplings

Starting from the mixing angle

$$\tan 2\theta = \frac{2\lambda_{SH}v_s v}{\lambda_S v_s^2 - \lambda_1 v^2} \tag{A.2}$$

we can rewrite it to

$$\lambda_1 = \lambda_S\frac{v_s^2}{v^2} - \frac{2\lambda_{SH}v_s}{v\tan 2\theta} \tag{A.3}$$

which we can plug into the mass squared $m_{h_1}^2$ to obtain

$$m_{h_1}^2 = \frac{1}{2}\left(\lambda_S v_s^2 - \frac{2\lambda_{SH}v_s v}{\tan 2\theta} + \lambda_S v_s^2 - \frac{2\lambda_{SH}v_s v}{\tan 2\theta\cos 2\theta}\right) \tag{A.4}$$

$$= \lambda_S v_s^2 - \lambda_{SH}v_s v\left(1 + \frac{1}{\cos 2\theta}\right)\frac{1}{\tan 2\theta} \tag{A.5}$$

$$= \lambda_S v_s^2 - \lambda_{SH}v_s v\cot\theta \tag{A.6}$$

Similarly we get for $m_{h_2}^2$

$$m_{h_2}^2 = \frac{1}{2}\left(\lambda_S v_s^2 - \frac{2\lambda_{SH} v_s v}{\tan 2\theta} + \lambda_S v_s^2 + \frac{2\lambda_{SH} v_s v}{\tan 2\theta \cos 2\theta}\right) \tag{A.7}$$

$$= \lambda_S v_s^2 - \lambda_{SH} v_s v \left(1 - \frac{1}{\cos 2\theta}\right) \frac{1}{\tan 2\theta} \tag{A.8}$$

$$= \lambda_S v_s^2 + \lambda_{SH} v_s v \tan\theta \tag{A.9}$$

With the masses we can rewrite λ_{SH}. Taking $m_{h_1}^2 - m_{h_2}^2$

$$m_{h_2}^2 - m_{h_1}^2 = \lambda_{SH} v_s v(\tan\theta + \cot\theta) \tag{A.10}$$

$$= 2\lambda_{SH} v_s v \csc 2\theta \tag{A.11}$$

and simplifying

$$\lambda_{SH} = \frac{m_{h_2}^2 - m_{h_1}^2}{2 v_s v \csc 2\theta} \tag{A.12}$$

$$= \frac{m_{h_2}^2 - m_{h_1}^2}{2 v_s v} \sin 2\theta. \tag{A.13}$$

We can now use this result to calculate λ_S. Starting from $m_{h_2}^2$

$$m_{h_2}^2 = \lambda_S v_s^2 + \left(\frac{m_{h_2}^2 - m_{h_1}^2}{2 v_s v}\right) \sin 2\theta \tan\theta v_s v \tag{A.14}$$

$$= \lambda_S v_s^2 + m_{h_2}^2 \sin^2\theta - m_{h_1}^2 \sin^2\theta \tag{A.15}$$

which is equivalent to

$$\lambda_S v_s^2 = m_{h_2}^2 - m_{h_2}^2 \sin^2\theta + m_{h_1}^2 \sin^2\theta \tag{A.16}$$

$$= m_{h_2}^2 \cos^2\theta + m_{h_1}^2 \sin^2\theta \tag{A.17}$$

that then gives the coupling

$$\lambda_S = \frac{1}{v_s^2} m_{h_2}^2 \cos^2\theta + \frac{1}{v_s^2} m_{h_1}^2 \sin^2\theta \tag{A.18}$$

A.3 The Beta functions as calculated by SARAH

The lower index signifies which coupling and the superscript loop order.

$$\begin{aligned}\beta_{\lambda_1}^{(1)} = &+\frac{27}{100} g_1^4 + \frac{9}{10} g_1^2 g_2^2 + \frac{9}{4} g_2^4 - \frac{9}{5} g_1^2 \lambda_1 - 9 g_2^2 \lambda_1 + 12\lambda_1^2 \\ &+ 2\lambda_{SH}^2 + 12\lambda_1 \mathrm{Tr}\left(Y_d Y_d^\dagger\right) + 4\lambda_1 \mathrm{Tr}\left(Y_e Y_e^\dagger\right) + 12\lambda_1 \mathrm{Tr}\left(Y_u Y_u^\dagger\right) \\ &- 12\mathrm{Tr}\left(Y_d Y_d^\dagger Y_d Y_d^\dagger\right) - 4\mathrm{Tr}\left(Y_e Y_e^\dagger Y_e Y_e^\dagger\right) - 12\mathrm{Tr}\left(Y_u Y_u^\dagger Y_u Y_u^\dagger\right)\end{aligned} \tag{A.19}$$

$$
\begin{aligned}
\beta^{(2)}_{\lambda_1} =& -\frac{3411}{1000}g_1^6 - \frac{1677}{200}g_1^4g_2^2 - \frac{289}{40}g_1^2g_2^4 + \frac{305}{8}g_2^6 + \frac{1887}{200}g_1^4\lambda_1 + \frac{117}{20}g_1^2g_2^2\lambda_1 \\
& - \frac{73}{8}g_2^4\lambda_1 + \frac{54}{5}g_1^2\lambda_1^2 + 54g_2^2\lambda_1^2 - 78\lambda_1^3 - 10\lambda_1\lambda_{SH}^2 + 8\lambda_{SH}^3 \\
& + \frac{1}{10}\Big(225g_2^2\lambda_1 - 45g_2^4 + 80\Big(10g_3^2 - 9\lambda_1\Big)\lambda_1 + 9g_1^4 + g_1^2\Big(25\lambda_1 + 54g_2^2\Big)\Big)\mathrm{Tr}\Big(Y_dY_d^\dagger\Big) \\
& - \frac{3}{10}\Big(15g_1^4 + 5\Big(16\lambda_1^2 - 5g_2^2\lambda_1 + g_2^4\Big) - g_1^2\Big(22g_2^2 + 25\lambda_1\Big)\Big)\mathrm{Tr}\Big(Y_eY_e^\dagger\Big) \\
& - \frac{171}{50}g_1^4\mathrm{Tr}\Big(Y_uY_u^\dagger\Big) + \frac{63}{5}g_1^2g_2^2\mathrm{Tr}\Big(Y_uY_u^\dagger\Big) - \frac{9}{2}g_2^4\mathrm{Tr}\Big(Y_uY_u^\dagger\Big) \\
& + \frac{17}{2}g_1^2\lambda_1\mathrm{Tr}\Big(Y_uY_u^\dagger\Big) + \frac{45}{2}g_2^2\lambda_1\mathrm{Tr}\Big(Y_uY_u^\dagger\Big) + 80g_3^2\lambda_1\mathrm{Tr}\Big(Y_uY_u^\dagger\Big) \\
& - 72\lambda_1^2\mathrm{Tr}\Big(Y_uY_u^\dagger\Big) + \frac{8}{5}g_1^2\mathrm{Tr}\Big(Y_dY_d^\dagger Y_dY_d^\dagger\Big) - 64g_3^2\mathrm{Tr}\Big(Y_dY_d^\dagger Y_dY_d^\dagger\Big) \\
& - 3\lambda_1\mathrm{Tr}\Big(Y_dY_d^\dagger Y_dY_d^\dagger\Big) - 42\lambda_1\mathrm{Tr}\Big(Y_dY_u^\dagger Y_uY_d^\dagger\Big) - \frac{24}{5}g_1^2\mathrm{Tr}\Big(Y_eY_e^\dagger Y_eY_e^\dagger\Big) \\
& - \frac{16}{5}g_1^2\mathrm{Tr}\Big(Y_uY_u^\dagger Y_uY_u^\dagger\Big) - 64g_3^2\mathrm{Tr}\Big(Y_uY_u^\dagger Y_uY_u^\dagger\Big) - 3\lambda_1\mathrm{Tr}\Big(Y_uY_u^\dagger Y_uY_u^\dagger\Big) \\
& - 24\mathrm{Tr}\Big(Y_dY_d^\dagger Y_dY_u^\dagger Y_uY_d^\dagger\Big) + 12\mathrm{Tr}\Big(Y_dY_u^\dagger Y_uY_d^\dagger Y_dY_d^\dagger\Big) \\
& + 20\mathrm{Tr}\Big(Y_eY_e^\dagger Y_eY_e^\dagger Y_eY_e^\dagger\Big) + 60\mathrm{Tr}\Big(Y_uY_u^\dagger Y_uY_u^\dagger Y_uY_u^\dagger\Big) \\
& - 12\mathrm{Tr}\Big(Y_dY_u^\dagger Y_uY_u^\dagger Y_uY_d^\dagger\Big) + 60\mathrm{Tr}\Big(Y_dY_d^\dagger Y_dY_d^\dagger Y_dY_d^\dagger\Big) - \lambda_1\mathrm{Tr}\Big(Y_eY_e^\dagger Y_eY_e^\dagger\Big) \qquad \text{(A.20)}
\end{aligned}
$$

$$
\beta^{(1)}_{\lambda_S} = 10\lambda_S^2 + 4\lambda_{SH}^2 \qquad \text{(A.21)}
$$

$$
\begin{aligned}
\beta^{(2)}_{\lambda_S} =& -60\lambda_S^3 + \frac{24}{5}g_1^2\lambda_{SH}^2 + 24g_2^2\lambda_{SH}^2 - 20\lambda_S\lambda_{SH}^2 + 16\lambda_{SH}^3 \\
& - 24\lambda_{SH}^2\mathrm{Tr}\Big(Y_uY_u^\dagger\Big) - 24\lambda_{SH}^2\mathrm{Tr}\Big(Y_dY_d^\dagger\Big) - 8\lambda_{SH}^2\mathrm{Tr}\Big(Y_eY_e^\dagger\Big) \qquad \text{(A.22)}
\end{aligned}
$$

$$
\begin{aligned}
\beta^{(1)}_{\lambda_{SH}} =& \frac{1}{10}\lambda_{SH}\Big(20\mathrm{Tr}\Big(Y_eY_e^\dagger\Big) + 40\lambda_S - 40\lambda_{SH} - 45g_2^2 \\
& + 60\lambda_1 + 60\mathrm{Tr}\Big(Y_dY_d^\dagger\Big) + 60\mathrm{Tr}\Big(Y_uY_u^\dagger\Big) - 9g_1^2\Big) \qquad \text{(A.23)}
\end{aligned}
$$

$$\begin{aligned}\beta^{(2)}_{\lambda_{SH}} =&\frac{1671}{400}g_1^4\lambda_{SH} + \frac{9}{8}g_1^2g_2^2\lambda_{SH} - \frac{145}{16}g_2^4\lambda_{SH} + \frac{36}{5}g_1^2\lambda_1\lambda_{SH} + 36g_2^2\lambda_1\lambda_{SH}\\
&- \frac{3}{5}g_1^2\lambda_{SH}^2 - 3g_2^2\lambda_{SH}^2 + 36\lambda_1\lambda_{SH}^2 + 24\lambda_S\lambda_{SH}^2 - 11\lambda_{SH}^3\\
&+ \frac{1}{4}\lambda_{SH}\Big(- 144\lambda_1 + 160g_3^2 + 45g_2^2 + 48\lambda_{SH} + 5g_1^2\Big)\mathrm{Tr}\Big(Y_dY_d^\dagger\Big)\\
&+ \frac{17}{4}g_1^2\lambda_{SH}\mathrm{Tr}\Big(Y_uY_u^\dagger\Big) + \frac{45}{4}g_2^2\lambda_{SH}\mathrm{Tr}\Big(Y_uY_u^\dagger\Big) + 40g_3^2\lambda_{SH}\mathrm{Tr}\Big(Y_uY_u^\dagger\Big)\\
&+ 12\lambda_{SH}^2\mathrm{Tr}\Big(Y_uY_u^\dagger\Big) - \frac{27}{2}\lambda_{SH}\mathrm{Tr}\Big(Y_dY_d^\dagger Y_dY_d^\dagger\Big) - 21\lambda_{SH}\mathrm{Tr}\Big(Y_dY_u^\dagger Y_uY_d^\dagger\Big)\\
&- \frac{27}{2}\lambda_{SH}\mathrm{Tr}\Big(Y_uY_u^\dagger Y_uY_u^\dagger\Big) - 36\lambda_1\lambda_{SH}\mathrm{Tr}\Big(Y_uY_u^\dagger\Big)\\
&- 15\lambda_1^2\lambda_{SH} - 10\lambda_S^2\lambda_{SH} + \frac{1}{4}\lambda_{SH}\Big(15g_1^2 + 15g_2^2 + 16\lambda_{SH} - 48\lambda_1\Big)\mathrm{Tr}\Big(Y_eY_e^\dagger\Big)\\
&- \frac{9}{2}\lambda_{SH}\mathrm{Tr}\Big(Y_eY_e^\dagger Y_eY_e^\dagger\Big) \qquad \text{(A.24)}\end{aligned}$$

A.4 Dark matter plots

We display here the wider range of parameters we scanned over. The ranges of parameters are given in table A.4. For the left plots the relic density is displayed as a copper color gradient with darker tones corresponding to lower relic densities. The correct relic density is $\Omega h^2 = 0.120 \pm 0.001$. It is however illustrative to consider the relic density as a contour plot to better understand the interplay between the parameters since the plots with the correct relic density give no such indication.

Varied	Range 1	Range 2
$\lambda_{SH}, m_{S_{DM}}$	$\lambda_{SH} \in [0, 0.3]$	$m_{S_{DM}} \in [0, 800]$GeV
λ_{SH}, λ_S	$\lambda_{SH} \in [0, 0.3]$	$\lambda_S \in [0, 2]$
λ_S, v_s	$\lambda_S \in [0, 1]$	$v_s \in]0, 1500]$GeV
$m_{S_{DM}}, v_s$	$m_{S_{DM}} \in [0, 1500]$GeV	$v_s \in [0, 2500]$GeV
λ_{SH}, v_s	$\lambda_{SH} \in [0, 0.1]$	$m_{S_{DM}} \in [0, 1500]$GeV
$\lambda_S, m_{S_{DM}}$	$\lambda_S \in [0, 0.3]$	$m_{S_{DM}} \in [0, 250]$GeV

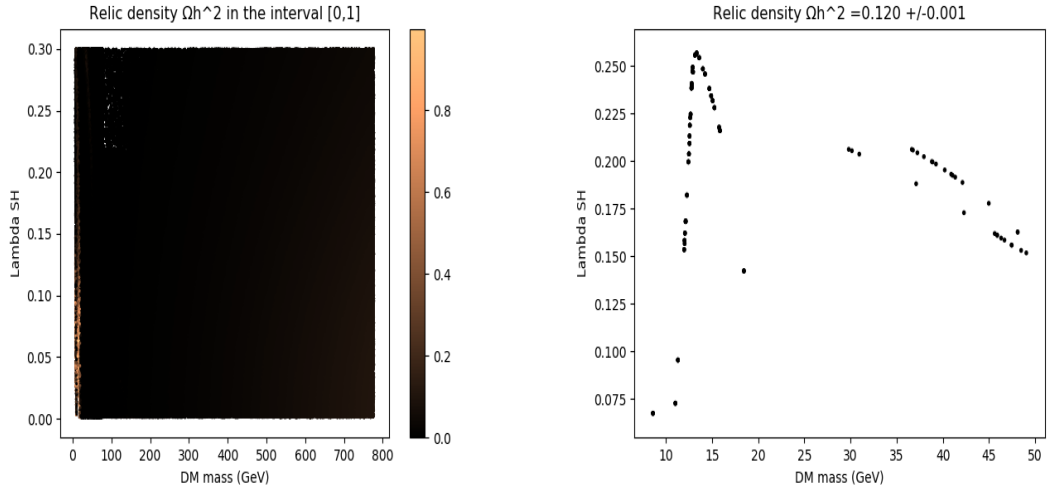

Figure A.1: Left: Variation of $\lambda_{SH} \in [0, 0.6]$ and $m_{DM} \in]0, 740\text{GeV}]$. Right: The parameters which give a correct relic density $\Omega h^2 \approx 0.120 \pm 0.001$.

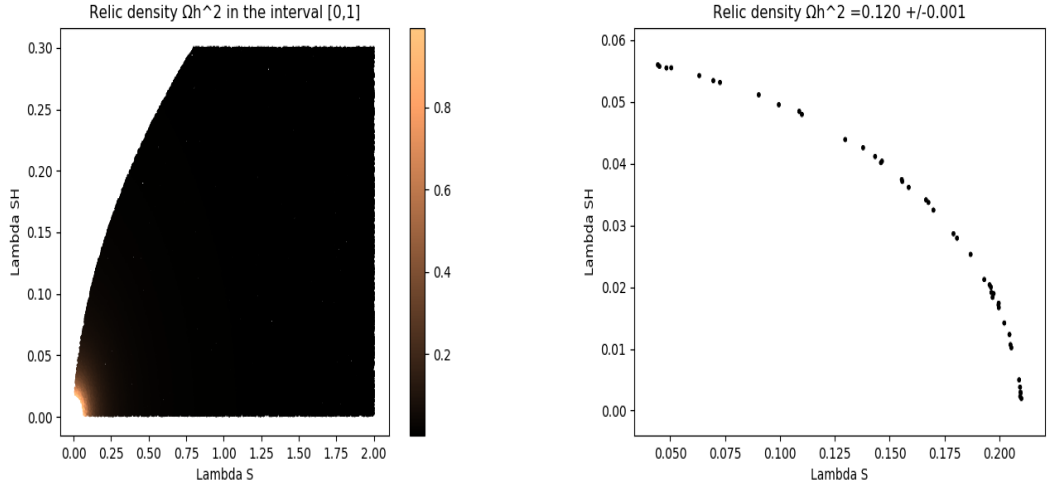

Figure A.2: Left: Variation of $\lambda_{SH} \in [0, 0.6]$ and $\lambda_S \in [0, 2]$. The white region to the left is due to violation of the condition $\lambda_1 \lambda_S > \lambda_{SH}^2$. At the origin we see that the relic density is more favorable than at high couplings. Right: Plotting the allowed parameters when we demand $\Omega h^2 \approx 0.120 \pm 0.001$.

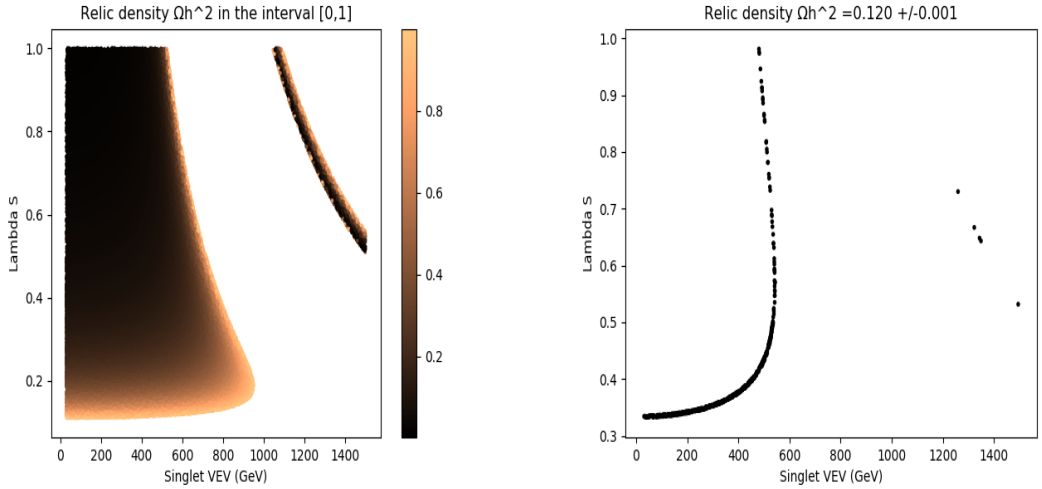

Figure A.3: Left: The relic density corresponding to variations of $\lambda_S \in [0, 2]$ and $v_s \in]0, 1500\text{GeV}]$. The white area in the middle is due to violation of $\lambda_1\lambda_S > \lambda_{SH}$ or due to $m^2_{h_2} < 0$. The relic densities in this case are discrete islands. Right: Showing only the correct values $\Omega h^2 \approx 0.120 \pm 0.001$ gives insight into how the coupling and VEV affect each other.

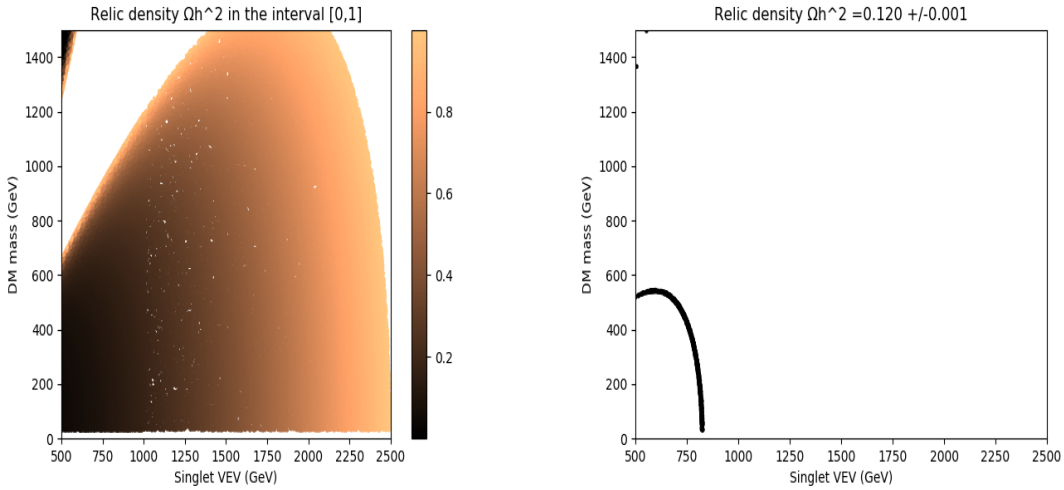

Figure A.4: Left: The relic density when we varied $m_{S_{DM}} \in [0, 15\text{TeV}]$ and $v_s \in [0, 2500\text{GeV}]$. Right: Plot of the parameters for which the relic density corresponds to measurements $\Omega h^2 = 0.120 \pm 0.001$.

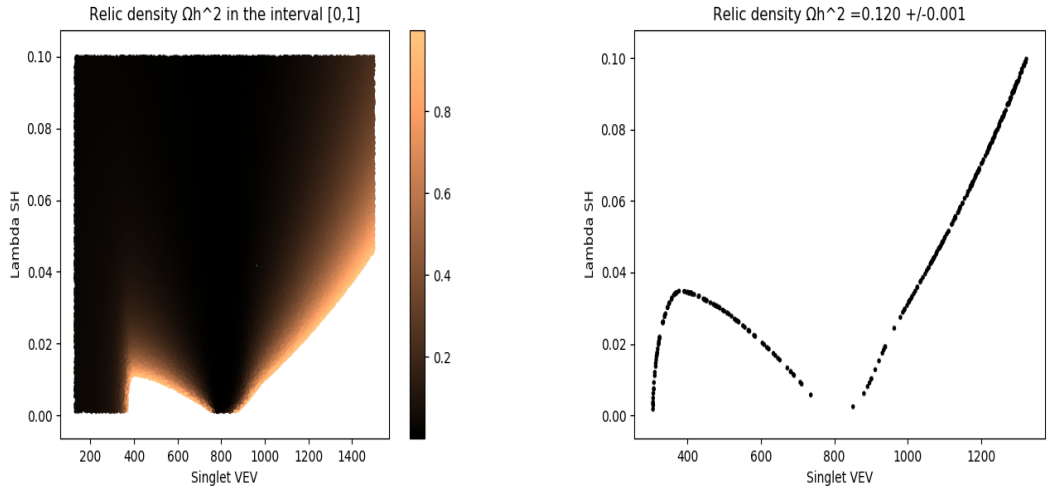

Figure A.5: Left: The relic density due to variations of $\lambda_{SH} \in [0, 0.2]$ and $v_s \in [0, 1500\text{GeV}]$. Right: The correct values for the relic density $\Omega h^2 = 0.120 \pm 0.001$ as a function of the parameters.

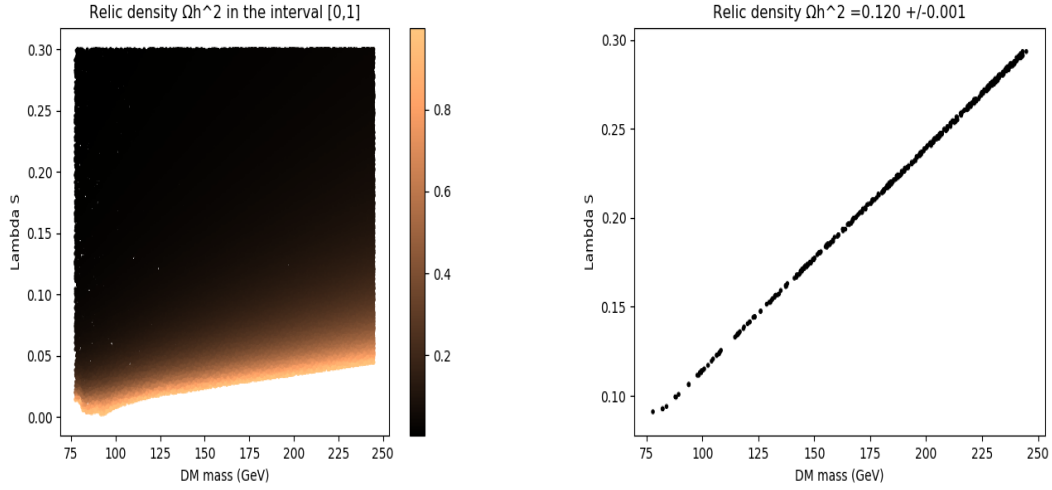

Figure A.6: Left: For $\lambda_S \in [0, 0.3]$ and the DM mass $m_{S_{DM}} \in [75\text{GeV}, 250\text{GeV}]$ the relic density appears to be linearly dependent on both parameters. Right: The parameters which give the correct relic density values $\Omega h^2 = 0.120 \pm 0.001$.

Bibliography

1 G. Aad, T. Abajyan, B. Abbott, J. Abdallah, S. Abdel Khalek, A. Abdelalim, O. Abdinov, R. Aben, B. Abi, M. Abolins, and et al., "Observation of a new particle in the search for the standard model higgs boson with the atlas detector at the lhc," Physics Letters B, vol. 716, p. 1–29, Sep 2012.

2 M. J. Herrero, "The standard model," 1998.

3 M. C. Gonzalez-Garcia, "Neutrino masses and mixing: A little history for a lot of fun," 2019.

4 J. Goldstone, A. Salam, and S. Weinberg, "Broken Symmetries," Phys. Rev., vol. 127, pp. 965–970, 1962.

5 F. Staub, "Sarah," 2008.

6 W. Porod and F. Staub, "Spheno 3.1: extensions including flavour, cp-phases and models beyond the mssm," Computer Physics Communications, vol. 183, p. 2458–2469, Nov 2012.

7 G. Belanger, F. Boudjema, and A. Pukhov, "micromegas : a code for the calculation of dark matter properties in generic models of particle interaction," 2014.

8 T. Ohl, "Drawing feynman diagrams with fx340-1 and metafont," Computer Physics Communications, vol. 90, p. 340–354, Oct 1995.

9 S. P. Martin, "Fermion self-energies and pole masses at two-loop order in a general renormalizable theory with massless gauge bosons," Physical Review D, vol. 72, Nov 2005.

10 M. Ciuchini, E. Franco, S. Mishima, and L. Silvestrini, "Electroweak precision observables, new physics and the nature of a 126 gev higgs boson," Journal of High Energy Physics, vol. 2013, Aug 2013.

11 A. Falkowski, C. Gross, and O. Lebedev, "A second higgs from the higgs portal," Journal of High Energy Physics, vol. 2015, May 2015.

12 J. D. Wells, "Tasi lecture notes: Introduction to precision electroweak analysis," 2005.

13 M. E. Peskin and T. Takeuchi, "Estimation of oblique electroweak corrections," 1991.

14 A. Ilnicka, T. Robens, and T. Stefaniak, "Constraining extended scalar sectors at the lhc and beyond," Modern Physics Letters A, vol. 33, p. 1830007, Apr 2018.

15 M. Baak, J. Cúth, J. Haller, A. Hoecker, R. Kogler, K. Mönig, M. Schott, and J. Stelzer, "The global electroweak fit at nnlo and prospects for the lhc and ilc," The European Physical Journal C, vol. 74, Sep 2014.

16 V. Khachatryan, A. M. Sirunyan, A. Tumasyan, W. Adam, T. Bergauer, M. Dragicevic, J. Erö, M. Friedl, R. Frühwirth, and et al., "Precise determination of the mass of the higgs boson and tests of compatibility of its couplings with the standard model predictions using proton collisions at 7 and 8 tev," The European Physical Journal C, vol. 75, May 2015.

17 A. Collaboration, "Search for scalar diphoton resonances in the mass range $65-600$ gev with the atlas detector in pp collision data at $\sqrt{s} = 8$ tev," 2014.

18 V. Khachatryan, A. M. Sirunyan, A. Tumasyan, W. Adam, T. Bergauer, M. Dragicevic, J. Erö, C. Fabjan, M. Friedl, and et al., "Observation of the diphoton decay of the higgs boson and measurement of its properties," The European Physical Journal C, vol. 74, Oct 2014.

19 V. Khachatryan, A. M. Sirunyan, A. Tumasyan, W. Adam, E. Asilar, T. Bergauer, J. Brandstetter, E. Brondolin, M. Dragicevic, and et al., "Search for a higgs boson in the mass range from 145 to 1000 gev decaying to a pair of w or z bosons," Journal of High Energy Physics, vol. 2015, Oct 2015.

20 S. Chatrchyan and V. e. a. Khachatryan, "Measurement of the properties of a higgs boson in the four-lepton final state," Physical Review D, vol. 89, May 2014.

21 G. e. a. Aad, "Measurements of higgs boson production and couplings in the four-lepton channel in pp collisions at center-of-mass energies of 7 and 8 tev with the atlas detector," Physical Review D, vol. 91, Jan 2015.

22 CMS Collaboration, "Search for the resonant production of two Higgs bosons in the final state with two photons and two bottom quarks," 4 2014.

23 G. e. a. Aad, "Search for higgs boson pair production in the yybb final state using pp collision data ats=8 tev from the atlas detector," Physical Review Letters, vol. 114, Feb 2015.

24 CMS Collaboration, "Search for di-Higgs resonances decaying to 4 bottom quarks," 8 2014.

25 Physics Letters B, vol. 565, p. 61–75, Jul 2003.

26 P. Aarnio et al., “"study of the leptonic decays of the z^0 boson",” Phys. Lett. B, vol. 241, pp. 425–434, 1990.

27 J. P. Lees and et al., “Search for di-muon decays of a low-mass higgs boson in radiative decays of the y(1s),” Physical Review D, vol. 87, Feb 2013.

28 J. T. e. a. Wei, “Measurement of the differential branching fraction and forward-backword asymmetry for b->k(*)l+l-,” Physical Review Letters, vol. 103, Oct 2009.

29 G. Aad and et al., “Measurement of higgs boson production in the diphoton decay channel in pp collisions at center-of-mass energies of 7 and 8 tev with the atlas detector,” Physical Review D, vol. 90, Dec 2014.

30 E. Corbelli and P. Salucci, “The extended rotation curve and the dark matter halo of m33,” Monthly Notices of the Royal Astronomical Society, vol. 311, p. 441–447, Jan 2000.

31 T. Lin, “Tasi lectures on dark matter models and direct detection,” 2019.

32 T. R. Slatyer, “Tasi lectures on indirect detection of dark matter,” 2017.

33 A. G. Riess, “The expansion of the universe is faster than expected,” Nature Reviews Physics, vol. 2, p. 10–12, Dec 2019.

34 P. Collaboration and N. A. et.al., “Planck 2018 results. vi. cosmological parameters,” 2018.

35 O. Piattella, “Lecture notes in cosmology,” UNITEXT for Physics, 2018.

36 J. M. Cline, “Tasi lectures on early universe cosmology: Inflation, baryogenesis and dark matter,” 2018.

37 M. J. de Oliveira, “Boltzmann stochastic thermodynamics,” Physical Review E, vol. 99, May 2019.

38 J. Bernstein, Kinetic Theory in the Expanding Universe. Cambridge Monographs on Mathematical Physics, Cambridge University Press, 1988.

39 D. Morrissey, “Lecture note 2: Thermal dark matter creation,” April 2012.

40 F. Staub, “Exploring new models in all detail with sarah,” Advances in High Energy Physics, vol. 2015, p. 1–126, 2015.

41 C. Gross, O. Lebedev, and T. Toma, “Cancellation mechanism for dark-matter–nucleon interaction,” Physical Review Letters, vol. 119, Nov 2017.

42 E. Aprile, J. Aalbers, F. Agostini, M. Alfonsi, L. Althueser, F. Amaro, M. Anthony, V. Antochi, F. Arneodo, L. Baudis, and et al., “Constraining the spin-dependent wimp-nucleon cross sections with xenon1t,” Physical Review Letters, vol. 122, Apr 2019.

43 J. Elias-Miró, J. R. Espinosa, G. F. Giudice, G. Isidori, A. Riotto, and A. Strumia, "Higgs mass implications on the stability of the electroweak vacuum," Physics Letters B, vol. 709, p. 222–228, Mar 2012.

44 G. Degrassi, S. Di Vita, J. Elias-Miró, J. R. Espinosa, G. F. Giudice, G. Isidori, and A. Strumia, "Higgs mass and vacuum stability in the standard model at nnlo," Journal of High Energy Physics, vol. 2012, Aug 2012.

45 "Measurement of the top-quark mass in t t-bar events with lepton+jets final states in pp collisions at sqrt(s)=tev," Tech. Rep. CMS-PAS-TOP-14-001, CERN, Geneva, 2014.

46 M. Neubert, "Les houches lectures on renormalization theory and effective field theories," 2019.

47 M. E. Peskin and D. V. Schroeder, An introduction to quantum field theory. Boulder, CO: Westview, 1995. Includes exercises.

48 T. Evans and D. Steer, "Wick's theorem at finite temperature," Nuclear Physics B, vol. 474, p. 481–496, Aug 1996.

49 I. M. Suslov, "On 't hooft's representation of the b-function," 2006.

50 S. Moch, "Precision determination of the top-quark mass," 2014.